Evolutionary unique *N*-glycan-dependent protein quality control system plays pivotal roles in cellular fitness and extracellular vesicle transport in *Cryptococcus neoformans*

Catia Mota[1], Kiseung Kim[1], Ye Ji Son[1], Eun Jung Thak[1], Su-Bin Lee[1], Ju-El Kim[2], Jeong-Kee Yoon[2], Min-Ho Kang[3,4], Heeyoun Hwang[5], Yong-Sun Bahn[6], J. Andrew Alspaugh[7], and Hyun Ah Kang[1*]

[1] Department of Life Science, Chung-Ang University, Seoul, 06974, Republic of Korea

[2] Department of Systems Biotechnology, Chung-Ang University, Anseong-Si, Gyeonggi-Do, 17546, Republic of Korea

[3] Department of Biomedical-Chemical Engineering, The Catholic University of Korea, Bucheon-Si, 14662, Republic of Korea

[4] Department of Biotechnology, The Catholic University of Korea, Bucheon-Si, 14662, Republic of Korea

[5] Digital OMICs Research Center, Korea Basic Science Institute, Cheongju-si, 28119, Republic of Korea

[6] Department of Biotechnology, Yonsei University, Seoul, 03722, Republic of Korea

[7] Department of Medicine, Duke University, Durham, North Carolina, USA

*For correspondence (H. A. K.) E-mail: hyunkang@cau.ac.kr; Tel.: +82-2-820-5863; Fax: +82-2-825-5206

Abstract

A conserved *N*-glycan-dependent endoplasmic reticulum protein quality control (ERQC) system has evolved in eukaryotes to ensure accuracy during glycoprotein folding. The human pathogen *Cryptococcus neoformans* possesses a unique *N*-glycosylation pathway that lacks the glucose addition step to the core *N*-glycan precursors in the ER but includes additional basidiomycetes-specific mannosidases. To investigate the molecular features and functions of the ERQC system in *C. neoformans*, we characterized a set of mutants with deletion of genes coding for the ERQC sensor UDP-glucose:glycoprotein glucosyltransferase (*UGG1*) and putative α1,2-mannose trimming enzymes (*MNS1*, *MNS101*, *MNL1*, and *MNL2*). The *ugg1*Δ, *mns1*Δ, *mns101*Δ, and *mns1*Δ*101*Δ mutants showed alterations in *N*-glycan profiles, defective cell surface organization, decreased survival in host cells, and varying degrees of reduced *in vivo* virulence. The *ugg1*Δ strain exhibited severely impaired extracellular secretion of capsular polysaccharides and virulence-related enzymes. Comparative transcriptome analysis showed the upregulation of protein folding, proteolysis, and cell wall remodeling genes, which is indicative of induced ER stress in *ugg1*Δ. However, no apparent changes were observed in the expression of genes involved in protein secretion or capsule biosynthesis. Additionally, extracellular vesicle (EV) analysis combined with proteomic analysis showed significant alterations in the number, size distribution, and cargo composition of EVs in *ugg1*Δ. These findings highlight the essential role of the functional ERQC system for cellular fitness under adverse conditions and proper EV-mediated transport of virulence bags, which are crucial for the full fungal pathogenicity of *C. neoformans*.

Keywords: *Cryptococcus neoformans*, glycoprotein quality control, UDP-glucose: glycoprotein glucosyltransferase, extracellular vesicles, pathogenicity

Introduction

Glycoproteins, destined for the secretory pathway, are synthesized on ribosomes attached to the surface of the endoplasmic reticulum (ER). They then enter the ER lumen where protein folding occurs (Rapoport, 2007). However, the accumulation of misfolded proteins affects cell viability and homeostasis; therefore, eukaryotes have evolved a conserved ER quality control (ERQC) system that recognizes folding defects, repairs them, and ensures the translocation of irreparable misfolded proteins into the cytosol for proteasome-mediated degradation via the ER-associated degradation (ERAD) system (Thibault and Ng, 2012; Xu and Ng, 2015; Balchin et al., 2016).

N-glycosylation is the most common post-translation modification, and the ERQC system relies on it to determine protein folding conformation (Aebi, 2013; Varki, 2017). Most eukaryotes synthesize a Dol-PP-linked $Glc_3Man_9GlcNAc_2$ oligosaccharide as a common core *N*-glycan, which attaches to nascent polypeptides in the ER via an asparagine residue. Then, glucosidases I and II (Gls1 and Gls2) remove two glucose residues from the core oligosaccharide, after which, the glycoproteins are transported from the ER to the Golgi apparatus. Proteins containing the core monoglucosylated *N*-glycans ($Glc_1Man_9GlcNAc_2$) enter a calnexin and/or calreticulin (CNX/CRT in mammals; CNE in yeast) chaperone-mediated folding cycle. Finally, Gls2 cleaves the remaining glucose residue. If the proteins are misfolded, they are recognized by the ERQC checkpoint enzyme, UDP-glucose:glycoprotein glucosyltransferase (UGGT), which reglucosylates them for re-entry into the folding cycle (Fig. 1A). Then, the *N*-glycans of the accurately folded proteins are further processed by Gls2 and α1,2-mannosidase I (Mns1) and moved to the Golgi apparatus. However, irreparably misfolded glycoproteins are targeted for ERAD. They undergo

demannosylation and retro-translocation for proteasomal degradation in the cytosol. Recently, *N*-glycan precursors in the ER of some protists and fungi were found to be shorter than the typical 14-sugar *N*-glycan precursors in most eukaryote organisms. The length of these *N*-glycan precursors significantly impacts *N*-glycan-dependent QC of glycoprotein folding and ERAD (Banerjee et al., 2007; Samuelson et al., 2015).

The basidiomycetous fungus *Cryptococcus neoformans* is an opportunistic, encapsulated human pathogen that primarily affects immunocompromised individuals, such as those with HIV/AIDS, causing fatal meningoencephalitis (Gottfredsson and Perfect, 2000; Kwon-Chung et al., 2000). The *N*-glycosylation pathway of *C. neoformans* is evolutionarily conserved; nevertheless, the structure and biosynthesis of its *N*-glycans shows several unique features (Park et al., 2012). *C. neoformans* contains serotype-specific high-mannose-type *N*-glycans with or without a β-1,2-xylose residue attached to the trimannosyl core. Additionally, the acidic *N*-glycans of *C. neoformans* contain xylose phosphates attached to the mannose residues both within the *N*-glycan core and outer mannose chains. The intact core *N*-glycan structure is crucial for *C. neoformans* pathogenicity (Thak et al., 2020); hence, alterations in the *N*-glycan structure modulates the interaction between the cell surface mannoproteins of *C. neoformans* and host cells (Lee et al., 2023). Unlike that observed in most eukaryotes, the *N*-glycosylation pathway in *C. neoformans* lacks homologous genes to *ALG6*, *ALG8*, and *ALG10*, which encode the glucosyltransferases that add three glucose residues to the core *N*-glycan before its attachment to proteins (Park et al., 2012). $Man_7GlcNAc_2$ and $Man_8GlcNAc_2$ without glucose residues are primarily detected in Dol-PP-linked glycans of *C. neoformans* (Samuelson et al., 2005). Moreover, the mature core *N*-glycan structures assembled on the cell surface mannoproteins of *C. neoformans* are primarily $Man_{6–7}GlcNAc_2$, which are shorter than the expected $Man_8GlcNac_2$ (Park et al., 2012). This observation led to the speculation that the terminal α-1,2-mannose residues of *C. neoformans N*-linked glycans may

be more susceptible to trimming by ER-1,2 mannosidases due to the lack of glucose residues compared to those of most eukaryotes. Alternatively, the presence of multiple 1,2 mannosidases may generate more extensively trimmed core *N*-glycans in *C. neoformans*.

Cryptococcus neoformans uses several virulence factors to evade the host immune system and enhance its pathogenicity. These include an extensive polysaccharide capsule composed of glucuronoxylomannan (GXM) and galactoxylomannan (GXMGal) (Doering et al., 2009; Zaragozza et al., 2009), melanin (Qiu et al., 2012; Zhu and Williamson, 2004), and various extracellular enzymes such as phosphatase and urease (Singh et al., 2013). These essential virulence factors are primarily transported within the EVs in *C. neoformans* (Casadevall et al., 2019; Rizzo et al., 2021; Rodrigues et al., 2007). Therefore, *C. neoformans* EVs represent a heterogeneous population of “virulence bags” containing numerous fungal survival and pathogenicity-associated molecules. Additionally, recent proteomics analysis of EV cargos has identified several cell surface glycoproteins including members of the CDA family, which are well-known immunomodulators (Rizzo et al., 2021; Spetch et al., 2017).

In this study, we report for the first time the molecular features and function of *N*-glycan-dependent ERQC in *C. neoformans* through a systematic analysis of mutant strains lacking a set of ERQC gene homologs. Notably, our results revealed the pivotal roles of the ERQC system not only in maintaining cellular fitness but also in the EV-mediated transport of virulence factors in *C. neoformans.*

Results

Evolutionary unique features of *C. neoformans* ERQC components

We performed BLAST analysis of the *C. neoformans* H99 genome to identify the ERQC pathway-associated homologous genes of *C. neoformans*, followed by comparison with the ERQC components in other eukaryotic organisms (Supplementary Fig. S1, A). Unlike most eukaryotes, several yeast species within the Ascomycota phylum, such as *Saccharomyces cerevisiae* and *Candida albicans*, do not possess a functional UGGT. In contrast, the UGGT homologs were identified in most fungal species belonging to Basidiomycota, including *C. neoformans* (Supplementary Fig. S1, A and B). The *C. neoformans* UGGT (CNAG_03648), which has been named as Ugg1, consists of 1,582 amino acids (aa) and features a signal peptide (1–20 aa) along with four tandem-like thioredoxin-like (TRXL) domains: TRXL12 (33–320 aa), TRXL13 (28–416 aa), TRXL14 (432–618 aa), and TRXL15 (712–950 aa). All these domains show a highly conserved structural organization. Ugg1 also contains a glucosyltransferase (GT) 24 domain with a DXD motif (1,369–1,371 aa) and a KDEL-like ER retention signal (1579–1582 aa), which facilitates its retrieval from the Golgi apparatus (Fig. 1B, Supplementary Fig. S2, A).

Additionally, we identified two *C. neoformans* ORFs, Mns1 (CNAG_02081) and Mns101 (CNAG_03240), as homologs of the eukaryote α1,2-mannosidase I, which processes *N*-glycans before exporting them to the Golgi. The *C. neoformans* Mns1 and Mns101 show 42.4% and 28.8% amino acid identities to *S. cerevisiae* ER- α1,2-mannosidase I, respectively, and share 30.9% identity between them. Furthermore, *C. neoformans* Mnl1 (CNAG_01987) and *C. neoformans* Mnl2 (CNAG_04498) were identified as putative components of ERQC in *C. neoformans* (Supplementary Fig. S1, A and C). Whereas *C. neoformans* Mnl1 is a homolog of the yeast α1,2-mannosidase-like protein (Htm1), which processes *N*-glycans that are re-directed towards ERAD, *C. neoformans* Mnl2 encodes a mannosidase that does not

show similarity to other eukaryotes mannosidases. Mns1, Mns101, and Mnl1 possess glucosyl hydrolase (GH) 47 domains, which are essential for mannosidase activity, whereas Mnl2 contains a GH92 domain, also known for its mannosidase activity (Fig. 1B). The Mns1 and Mnl1 protein families are characterized by the presence of a conserved cysteine (Cys) and alanine (Ala) residue (Jakob et al., 2001). These residues are located within the activity domain of cryptococcal Mns1, Mns101 and Mnl1, but not of Mnl2 (Supplementary Fig. S2, B). Notably, Mns101 and Mnl2 have been identified only in Basidiomycota yeasts (Supplementary Fig. S1, A) and seem to have diverged early from other mannosidase clades in the phylogenetic tree of fungal mannosidases (Supplementary Fig. S1, C). This indicates that Mns101 and Mnl2 are basidiomycete-specific proteins.

To examine the changes in ERQC-related gene expression under stress conditions, *C. neoformans*, which was cultivated in the presence of tunicamycin (TM, 5 μg/ml) or dithiothreitol (DTT, 20 mM) at 37 °C for 1 h, was subjected to quantitative reverse transcription-PCR (qRT-PCR) analysis (Fig. 1C). The analysis showed that *KAR2*, which encodes for a molecular chaperone associated with the unfolded protein response (UPR) system, was upregulated in response to inhibition of *N*-glycosylation by TM treatment, blockage of disulfide bond formation by DTT treatment, and heat stress at 37 °C. The ERQC components *UGG1*, *MNS1*, *MNS101*, *MNL1*, and *MNL2* were upregulated by DTT treatment; however, they were not significantly induced after 1 h of TM treatment. Under high-temperature conditions, only *UGG1* and *MNL2* exhibited an induced expression pattern. Notably, DTT treatment, which results in rapid accumulation of misfolded proteins in the ER, induced a 10-fold higher expression of *MNS1* and *MNL1*. These results strongly suggest that the *C. neoformans* genes *UGG1*, *MNS1*, *MNS101*, *MNL1*, and *MNL2* are crucial components of the ERQC and ERAD systems.

Loss of *UGG1*, *MNS1*, and *MNS101* causes alteration of *N*-glycan profiles in *C. neoformans*

We performed high-performance liquid chromatography (HPLC) analysis of the cell wall mannoproteins (cwMPs) from both the wild-type (WT) and ERQC mutant strains to investigate the ERQC malfunction-induced structural differences in *N*-glycans (Fig. 2). The HPLC profiles of cwMPs from the WT strain showed an M8 peak as the major species. This peak corresponded to *N*-glycans with 8 mannose residues (Fig. 2A, top). The glycan structure at the M8 peak ($Man_8GlcNAc_2$) in the WT primarily corresponded to the $Man_7GlcNAc_2$ core *N*-glycan with an additional mannose residue that is linked via an α1,6-linkage and added in the Golgi apparatus (Park et al., 2012). In the *ugg1*Δ mutant, M8 was also the main *N*-glycan species, but the pools of hypermannosylated *N*-glycans (larger than the M11 peak) were markedly reduced (Fig. 2A, middle). The altered *N*-glycan profile of the *ugg1*Δ mutant was restored to that of the WT after complementation with the WT *UGG1* gene (Fig. 2A, bottom). Additionally, lectin blotting of the extracellularly secreted proteins from WT and *ugg1*Δ strains showed a distinct increase in the quantity of lower molecular weight secretory glycoproteins in the *ugg1*Δ strain compared with that of the WT (Fig. 2B). These results suggest that Ugg1 function is essential for the hypermannosylation of *N*-glycans that occurs in the Golgi apparatus.

The *mns1*Δ mutant *N*-glycan profile showed a peak shift from an M8 to an M9 form, which strongly indicates that *C. neoformans* Mns1 could be the well-known ER α1,2-mannosidase I (Fig. 2C, *mns1*Δ). Notably, the loss of Mns101, which is present only in Basidiomycota, increased the fractions containing hypermannosylated glycans (> M10) while maintaining M8 as a primary core *N*-glycan form. This suggests that the basidiomycete-specific Mns101 may potentially be a novel α1,2-mannosidase that functions to remove mannose residues from hypermannosylated *N*-glycans in the Golgi apparatus or further trims

the M8 glycan in the ER before the glycoproteins are transported to the Golgi (Fig. 2C, *mns101*Δ). The matrix-assisted laser desorption ionization-time of flight (MALDI-TOF) mass spectrometer analysis of neutral *N*-glycans, collected from HPLC fractionation (Fig. 2C), further confirmed the shift of the major M8 peak in the WT strain to M9 in the *mns1*Δ mutant and the increase in the hypermannosylation profile in the *mns101*Δ mutant (Fig. 2D). The *N*-glycan profiles of the *mns1*Δ*101*Δ double mutant showed the combined effect of each null mutation, and it showed both increased hypermannosylated glycans and a shift from the M8 to the M9 peak in both the HPLC (Fig. 2C, *mns1*Δ*101*Δ) and MALDI-TOF analyses. This indicates that Mns1 and Mns101 serve as mannosidases and play independent roles at different stages of *N*-glycan processing in *C. neoformans*.

In contrast, the loss of both *MNL1* and *MNL2* did not show notable differences in the HPLC profile of *N*-glycans from cell surface mannoproteins (Supplementary Fig. S3, A). Considering the expected function of Mnl1 and Mnl2 in ERAD, their substrates are mostly misfolded proteins that have not been transported to the Golgi apparatus. Thus, we speculate that only the normally processed *N*-glycan profiles of cell surface mannoproteins in the *mnl1*Δ *mnl2*Δ mutant strain were observed.

Loss of ERQC components results in defective growth fitness and increased stress sensitivity

We investigated the growth of the *ugg1*Δ mutant under various stress-inducing conditions to elucidate the roles of the ERQC components in ER stress response and adaptation, which are closely associated with *C. neoformans* virulence. The *ugg1*Δ mutant showed impaired growth even under normal growth conditions (Fig. 3A) and increased sensitivity to ER stress-inducing agents such as DTT, TM and cell wall stressors such as calcofluor white (CFW),

Congo red (CR), sodium dodecyl sulfate (SDS), and caffeine. Additionally, *ugg1*Δ showed hindered growth in the presence of antifungal drugs such as azole agents (fluconazole and ketoconazole) and the glucose transport inhibitor fludioxonil. These findings suggest that Ugg1 is crucial for the robust growth and survival of *C. neoformans* under various stress conditions. In contrast, the single deletion strains (*mns1*Δ and *mns101*Δ) and double deletion strain *(mns1*Δ*101*Δ) did not exhibit noticeable phenotypic changes except for a slight increase in sensitivity of *mns101*Δ and *mns1*Δ*101*Δ to higher fludioxonil concentrations (Fig. 3B). Similarly, neither the single nor double disruption of *MNL1* and *MNL2* produced detectable changes in the tested growth phonotypes of *C. neoformans* cells (Supplementary Fig. S3, B).

To determine whether the defective *ugg1*Δ phenotypes were induced partially by ER stress caused by the accumulation of misfolded proteins, we performed a growth analysis in the presence of 5',5',5'-trifluoroleucine (TFL), which is a leucine analog (Fig. 3C). We hypothesized that TFL incorporation into proteins could cause improper folding, which would ultimately negatively impact cell growth. *ugg1*Δ showed noticeably inhibited growth in the presence of TFL, whereas the WT strain showed no growth inhibition. The *mns1*Δ*101*Δ strain also exhibited slightly increased sensitivity to TFL compared with that of the WT strain. As a defense mechanism against misfolded protein accumulation-mediated ER stress, UPR is induced by the unconventional splicing of the *HXL1* transcription factor in *C. neoformans* (Cheon et al., 2011). RT-PCR analysis showed that spliced *HXL1* level was significantly higher in the *ugg1*Δ strain compared with that of WT, even under normal culture conditions (Fig. 3D). Moreover, enhanced *HXL1* splicing in *ugg1*Δ strongly suggests that *UGG1* loss results in misfolded protein accumulation, which causes ER stress even under normal growth conditions. Furthermore, green fluorescence protein (GFP)-tagged Ugg1, Mns1, and Mns101 proteins colocalized with the ER marker, confirming them to be functional ERQC components based on their subcellular localization in the ER (Fig. 3E).

ERQC defects lead to virulence attenuation in *C. neoformans*

We investigated the effects of a defective ERQC on *in vitro* virulence phenotypes of *C. neoformans* by analyzing cryptococcal capsule and melanin pigment production, as these are the two of the major virulence factors of *C. neoformans*. Culturing on L-DOPA-containing plates showed that melanin production was lower in the *ugg1*Δ strain compared with that in the WT (Fig. 4A). In contrast, the *mns1*Δ*101*Δ mutant cells did not show detectable defects in melanin production at either 30 or 37 °C (Fig. 4B). India ink staining of the capsule showed significantly reduced capsule thickness in the *ugg1*Δ strain and a moderate defect in the *mns1*Δ*101*Δ strain (Fig. 4C).

Defects in the ERQC system led to a more apparent decrease in pathogenicity in a murine model of systemic cryptococcosis. Notably, the *ugg1*Δ strain was completely avirulent *in vivo* (Fig 4D), and the infected animals did not display any signs of illness. Furthermore, *MNS1* and *MNS101* single disruptions did not cause a detectable decrease in *C. neoformans* pathogenicity; however, their double disruption resulted in decreased virulence. Histopathological analysis of infected mice lungs showed significantly reduced lung colonization by both *ugg1*Δ and *mns1*Δ*101*Δ cells (Supplementary Fig. S4, A). Additionally, the fungal burden of *ugg1*Δ-infected animals showed a notable decrease in organ colonization at 60 days post-infection (dpi) (Supplementary Fig. S4, B). Analysis of the fungal burden at 7 dpi showed significantly reduced organ colonization of the *mns1*Δ*101*Δ mutant compared with that of the WT (Supplementary Figure S4, C). Next, we co-cultured the mutant strains with the macrophage-like cell line J447A.1 to investigate the effects of ERQC defects on cryptococcal survival within macrophages (Fig. 4E). Consistent with the *in vivo* survival data, the number of surviving *ugg1*Δ and *mns1*Δ*101*Δ cells within macrophages was significantly

lower compared with that of the WT strain. These data prove that a functional ERQC system is critical for maintaining full *in vivo* pathogenicity and ensuring robust survival within host immune cells.

Loss of Ugg1 function manifests defects in extracellular transport of GXM

Cryptococcal capsule materials are synthesized intracellularly and secreted to the cell surface. Subsequently, they are assembled and bound to the cell wall (Yoneda and Doering, 2006). The observed capsule defects in the *ugg1*Δ and *mns1*Δ*101*Δ mutant strains may be attributed to issues in the capsule polysaccharide synthesis or transport steps. Alternatively, defective capsule formation may result from increased shedding of capsule polymers without proper attachment to the cell surface. To determine the cause of the capsule defects, we examined the amounts of capsular polysaccharides synthesized intracellularly and those shed into the culture supernatant by a capsule blotting assay. We used the GXM-specific antibody 18B7 to analyze the WT and ERQC mutant strains, together with the *cap59*Δ and *rim101*Δ strains, which exhibit capsule formation defects. GXM is a major capsule component comprising α1,3-linked mannose residues with xylosyl and glucuronyl side groups. The *cap59*Δ strain lacks a visible capsule because of a defect in GXM synthesis (Grijpstra et al., 2009). *C. neoformans rim101*Δ exhibits a hypocapsular phenotype because of defective capsule attachment, despite normal polysaccharide synthesis and secretion (O'Meara et al., 2010). Intracellular GXM quantities did not notably differ between the WT, *ugg1*Δ, *mns1*Δ*101*Δ, and *rim101*Δ strains, although *ugg1*Δ showed slightly reduced GXM level (Fig. 5A, left). In contrast, no intracellular GXM was detected in *cap59*Δ, which was consistent with its defect in GXM synthesis. Moreover, the *ugg1*Δ strain did not show shedding of capsule polymers, whereas the *mns1*Δ*101*Δ strain showed shedding of GXM-containing polymers that were

shorter in length than the WT-type polymers. This indicates poor polysaccharide polymerization (Fig. 5A, right). Reduced capsule thickness in *mns1*Δ*101*Δ is consistent with previous reports that capsule size is mediated at the polymer level (Yoneda et al., 2008). Therefore, these results suggest that *ugg1*Δ contains a defect in polysaccharide trafficking to the extracellular space, whereas *mns1*Δ*101*Δ contains a defect in polysaccharide polymerization, which results in defective capsule elaboration, albeit with differential degrees of severity in both ERQC mutants.

Furthermore, to determine whether the ERQC mutants are also impaired in capsule attachment, we performed a capsule transfer assay, which is a technique that assesses whether exogenously shed capsule polysaccharides bind to acapsular mutants (Reese and Doering, 2003). The hypocapsular *rim101*Δ mutant did not show reassociation of capsular polysaccharides; however, the acapsular *cap59*Δ mutant showed recovery of capsule formation when co-incubated with exogenous GXM (Fig. 5B). Similarly, *ugg1*Δ reverted its acapsular phenotype on incubation with the WT-shed polysaccharides, which strongly suggests that the defective capsule phenotype of *ugg1*Δ is primarily due to defective GXM synthesis or secretion rather than impaired attachment of capsule polymers. We further conducted a capsule transfer assay using capsular polysaccharides shed from *mns1*Δ*101*Δ. The *cap59*Δ mutant reverted to the capsular phenotype by attaching to the *mns1*Δ*101*Δ-shed polymers. However, the fluorescence intensity of the capsule generated by the *mns1*Δ*101*Δ-shed polymers was significantly lower than that of the cells attached with polysaccharides obtained from the WT. This result suggests that the *mns1*Δ*101*Δ double mutant secretes incomplete capsule polysaccharides (Fig. 5C), which leads to a hypocapsular phenotype. These results collectively indicate that the defective GXM trafficking to the extracellular space is caused by disruptive ERQC, impairing capsule formation.

Transmission electron microscopy (TEM) imaging of the WT and mutant cells distinctly showed a diminished capsule structure and loss of capsule shedding in the *ugg1*Δ strain compared with that of the WT strain (Fig. 5D). Additionally, we observed considerable thinning of the cell walls in both ERQC mutant cells. Notable changes in intracellular structures along with an increase in the number of pigmented vesicles were observed in the mutant cells even under YPD culture conditions. Under capsule-inducing conditions, a significant accumulation of vesicular structures (electron-lucent structures) was observed inside the cells, particularly in *ugg1*Δ. We performed LD staining to determine whether these vesicular structures might be lipid droplets (LDs). We observed a notable increase in LDs in *ugg1*Δ under capsule-inducing culture conditions (Supplementary Fig. S5, A). LDs impact proteostasis by sequestering misfolded proteins intended for degradation and providing an "escape hatch" when the ERQC is overloaded (Ploegh, 2007; Vevea et al., 2015). Additionally, FM4-64 dye staining showed increased number of vacuoles in the *ugg1*Δ cells compared with that in the WT (Supplementary Fig. S5, B). Moreover, all the observed abnormal phenotypes were less pronounced in the *mns1*Δ*101*Δ mutant than in the *ugg1*Δ strain. Taken together, the altered vesicular structures observed in the *ugg1*Δ and *mns1*Δ*101*Δ strains indicate that the ERQC function is crucial for maintaining proper vesicular structure and cell surface organization as both these functions are closely associated with the extracellular trafficking of virulence factors and cell wall remodeling.

_ugg1_Δ transcriptomic profiling shows induced ER and cell wall integrity stress responses

To elucidate the mechanisms underlying *UGG1* deletion-induced physiological changes in *C. neoformans*, we performed RNA sequencing (RNAseq)-based transcriptome analysis of the

335 WT and *ugg1*Δ strains under standard growth conditions (YPD medium, 30 °C). Differential
336 gene expression analysis was performed with focus on changes exceeding 2-fold between the
337 WT and *ugg1*Δ mutant strains (Fig. 6A). Comparative transcriptome analysis showed
338 significant alterations in the expression patterns of 146 genes, of which 85 were upregulated
339 and 61 were downregulated compared with that of the WT strain (Fig. 6B, Supplementary
340 Tables S2, A and B).

341 Notably, the *ugg1*Δ mutant showed upregulation of genes such as *SKN1* and *KRE6*
342 (transmembrane glucosidases involved in the sphingolipid biosynthesis and β-glucan
343 biosynthesis), *CAT2* (a putative peroxisomal catalase), *CHS7* (chitin synthase export
344 chaperone), and CNAG_05458 (a putative endo-1,3(4)-β-glucanase). In contrast, genes
345 encoding *ERG3* and *ERG25* (associated with the ergosterol biosynthesis pathway) and *FHB1*
346 (flavohemoglobin denitrosylase associated with counteracting nitric oxide stress) were
347 significantly downregulated. Gene Ontology (GO) analysis in *ugg1*Δ showered pronounced
348 induction of genes implicated in various cellular processes, including the hydrolysis of *O*-
349 glycosyl compounds for cell wall remodeling, DNA replication, proteolysis, ribosome
350 biogenesis, protein folding, and serine/threonine kinase activity. In contrast, the genes
351 associated with carbohydrate and lipid metabolism, chaperone binding, iron homeostasis, and
352 mitochondrial intermembrane space were considerably downregulated (Fig. 6C). The
353 transcriptome profile strongly suggests that loss of Ugg1 function induces the expression of
354 several genes involved in maintaining cell wall integrity to compensate for cell wall defects,
355 particularly those associated with chitin (*CDA2*, *CHS7*, *QRI1*, and CNAG_06898) and glucan
356 biosynthesis (*SKN1*, *KRE6*, *EBG1*, *LPI9*, CNAG_05458, and *BLG2*). Furthermore, genes
357 coding for ER chaperones that aid in protein folding (*ERO1*, *KAR2*, *LHS1*, and *PDI1*) and
358 chaperone regulator (*SCJ1*), and genes involved in proteolysis in the ER (CNAG_04635,

CNAG_06658) were induced, likely as part of the ER stress response induced by the accumulation of misfolded proteins in the presence of a defective ERQC.

Further investigation of the effects of *UGG1* disruption in the expression of genes involved in capsule biosynthesis, cell wall remodeling, and the secretion pathways of protein virulence factors using qRT-PCR analysis (Fig. 6D) showed no noticeable repression of the expression of genes related to capsule biosynthesis and conventional or unconventional secretion pathways at the mRNA level, despite the aberrantly displayed defective phenotypes. Notably, *ugg1*Δ mutant showed notable upregulation of the genes involved in cell wall remodeling, as indicated by the GO analysis of transcriptome data. Taken together, these data strongly suggest that ERQC system malfunction caused by *UGG1* disruption may exert negative effects on the production of virulence factors at post-transcriptional levels, most likely during the extracellular transport process.

EV-mediated protein trafficking and non-conventional secretion is impaired in the *ugg1*Δ mutant strain

Many enzymes contribute to the composite cryptococcal virulence phenotype. Some of these virulence-associated enzymes are secreted through traditional secretion pathways, whereas others are packaged into EVs and released into the extracellular milieu via non-conventional secretion mechanisms (Amelida et al., 2015). The defects observed in the ERQC mutant strains, particularly in the production of melanin and polysaccharide capsules, both of which are primarily transported by EVs, suggest a possible impairment in the EV-mediated extracellular transport of virulence-associated enzymes such as acid phosphatase, urease, and laccase (Rodrigues et al., 2008) in these mutants. Laccase enables melanin synthesis (Salas et al., 1996), urease hydrolyzes urea into ammonia, which facilitates *C. neoformans* invasion

383 into the CNS (Olszewski et al., 2014), and acid phosphatase serves as an adhesion-related
384 enzyme (Collopy-Junior et al., 2006). Therefore, we examined the *in vitro* activity of these
385 virulence-related enzymes in both intracellular and extracellular secreted fractions.

386 Comparative analysis showed that whereas the changes in the intracellular activities of
387 acid phosphatase, urease, and laccase were negligible, their activities were significantly low
388 in the extracellular fractions of the *ugg1*Δ cells (Fig. 7A, 7B, 7C, and 7D). Urease analysis
389 was performed in both solid and liquid media, and it showed a notable loss of secreted urease
390 activity in *ugg1*Δ cells with a slight decrease in the *mns1*Δ*101*Δ double mutant cells (Fig. 7A
391 and 7B). As urease lacks a signal peptide required for conventional protein secretion, low
392 urease secretion strongly indicates a compromised EV-mediated non-conventional secretory
393 pathway in the *ugg1*Δ mutant strain.

394 Next, we tested cellulase and α-amylase activities to assess the impact of disrupted
395 ERQC system on the conventional secretion pathway of non-virulence-related enzymes (Fig.
396 7E and 7F). The activities of these carbohydrate polymer-degrading enzymes in the
397 extracellular fraction of *ugg1*Δ were slightly lower than those of the WT; this likely indicates
398 decreased intracellular production rather than significantly compromised secretion efficiency.
399 Furthermore, we investigated the localization of chitin deacetylase I (Cda1), which is a
400 glycosylphosphatidylinositol (GPI)-anchored protein that is involved in the conversion of
401 chitin to chitosan for proper maintenance of cell wall integrity (Baker et al., 2007; Baker et
402 al., 2011; Upadhya et al., 2021). Cda1 was predominantly detected in the insoluble cellular
403 protein fraction, which includes the cell wall and membranes (Fig. 7G, left). This result is
404 consistent with the localization of Cda1 on the cell surface via a GPI anchor. Cda1 is secreted
405 extracellularly on cleavage of the GPI anchor. Notably, the *ugg1*Δ mutant strain shows much
406 higher intracellular and extracellular Cda1 levels compared with that of the WT and
407 *mns1*Δ*101*Δ strains (Fig. 7G, right). This concurs with the approximate 1.87-fold increase in

CDA1 mRNA levels observed in the RNAseq data. Thus, the efficient surface localization and secretion of Cda1 strongly support the conclusion that the conventional secretion pathway remains functional without significant compromise in *ugg1*Δ.

The acapsular mutant *cap59*Δ strain was previously reported to have secretion defects, based on observations that the *cap59*Δ strain generated in the serotype D background (*C. deneoformans*) displayed defective secretion of enzymes involved in the hydrolysis of raffinose or urease (Garcia-Rivera et al., 2004). However, the *cap59*Δ strain used in this study, which was constructed from the serotype A strain H99 background (Thak et al., 2020), showed defective alkaline phosphatase secretion but only marginally defective urease secretion. The *cap59*Δ acapsular mutant constructed from the *C. deneoformans* background does not use raffinose as a carbon source because of poor protein secretion of raffinose hydrolyzing enzymes (Garcia-Rivera et al., 2004). Therefore, to test whether the ERQC-related mutant strains utilize raffinose as a carbon source, we performed a growth test using SC media containing raffinose as the sole carbon source. Notably, *ugg1*Δ and *cap59*Δ strains showed no evident defects in raffinose utilization compared with that of the WT (Fig. 7H). This suggests that the conventional secretion pathway is functional in both mutant strains. Overall, the results suggest that the UGGT-mediated ERQC defect exerts a more pronounced negative impact on EV-mediated protein transport and only a marginal effect on the conventional secretion pathway.

Extracellular vesicle biogenesis and cargo loading are defective in *ugg1*Δ strain

We analyzed the number and size distribution of EVs to determine if defects in the assembly and transport of EVs in the *ugg1*Δ mutant might cause abnormal EV-mediated trafficking of virulence factors. Nanoparticle tracking analysis (NTA) showed a major peak in size

distribution at approximately 150 (134±28) nm in the WT strain, which was similar in size to mammalian exosomes and typical microbial EVs. Additionally, a minor peak ranging from 300–500 nm was observed and corresponded to the microvesicles (Fig. 8A). Notably, the size distribution of *ugg1*Δ EVs was more heterogeneous with smaller EVs ranging from 50–150 nm (82±16; 124±14) compared with that of the WT. The *cap59*Δ EVs displayed a major distribution of approximately 150 nm (120±21); however, the microvesicles were barely detected in either *cap59*Δ or *ugg1*Δ strains.

We observed a significant reduction in the total number of secreted EVs in the *ugg1*Δ mutant (approximately 40%), which suggests defective EV biogenesis or stability in the absence of functional Ugg1 (Fig. 8B). Cryo-TEM analysis of EV morphology confirmed that the sizes of EVs released by *ugg1*Δ were significantly smaller and more diverse than those of the WT or the acapsular mutant (Fig. 8C); this further supports the NTA results. Examining EV size distribution by measuring their diameter (Fig. 8D) further confirmed that although the EVs in the WT strain ranged from approximately 50–550 nm in size with distribution primarily concentrated at approximately 150 nm, the EVs in the *ugg1*Δ mutant were smaller (< 100 nm) with heterogeneous sizes. Notably, *cap59*Δ EVs were uniformly distributed at approximately 150 nm and were present at a higher concentration than those of EVs from the WT. An increase in EV release and virulence factors has been also observed in acapsular mutant strains of *C. neoformans* and *C. gattii* (Rodrigues et al., 20007; Reis et al., 2019), which supports the notion that the capsule serves as a barrier in EV release in capsule forming species.

To examine the protein content in EVs from WT and *ugg1*Δ, EV-associated proteins were extracted in triplicate using 8 M urea from purified EVs, and the equivalent concentration of EV proteins were subjected to proteomics analysis (Fig. 8E; Supplementary

Fig. S6, A). We identified 1,688 proteins and quantified 1,625 proteins (Supplementary Table S3). Among them, 1,008 proteins showed differences between WT and *ugg1*Δ (Supplementary Fig. S6, B). Compared with that of the WT EVs, the *ugg1*Δ EVs exhibited altered protein abundance with only 64 proteins showing upregulation and 777 proteins showing > 2-fold downregulation (Supplementary Fig. S6, C, D). Three proteomic analyses of *C. neoformans* EVs have been reported previously (Rodrigues et al., 2008; Wolf et al., 2014; Rizzo et al., 2021), identifying 76, 202, and 1,847 proteins associated with EVs in *C. neoformans*, respectively. Using the same culture medium and EV preparation method, the number and content of identified EV-associated proteins in our study was mostly similar to that reported by Rizzo et al., who further defined 71 non-ribosomal proteins as EV-enriched proteins after proteomic data enrichment analysis (Rizzo et al., 2021). We compared the protein content between WT and *ugg1*Δ among the EV proteins identified in our study with focus on the proteins commonly detected among either the 71 non-ribosomal EV-enriched proteins (Rizzo et al., 2021) or 50 overlapped proteins from two *C. neoformans* EV proteomic data sets reported by Rodrigues et al. and Wolf et al. (Bleackley et al., 2021). Among 59 EV-associated proteins that were commonly detected by previous and current studies, 24 proteins were detected at lower concentration, whereas 5 were present in higher concentrations of 2-fold difference in *ugg1*Δ mutant EVs compared with that of WT EVs (Fig. 8E; Supplementary Table S4). Thus, the proteome analysis showed that the absence of functional Ugg1 not only caused morphological alterations and reduced EV numbers but also altered EV protein abundance in *C. neoformans*.

To examine the loading defect of GXM in the *ugg1*Δ EVs, we examined the presence of GXM in purified EVs samples and compared the detected GXM quantities in the total cell extracts from WT, *ugg1*Δ, and *cap59*Δ strains (Fig. 8F). Cda1 was used as the representative EV-associated protein because the presence of Cda1 was reported within the *C. neoformans*

EV membrane despite a substantial portion of Cda1 being secreted through the conventional secretion pathway (Rizzo et al., 2021). The 8 M urea extracts were obtained from the purified EVs and the whole cells that were subjected to pelleting during EV purification. The extracted samples, which contained equivalent protein concentrations, were subjected to blotting analysis using GXM-specific (18B7) and Cda1-specific antibodies (Fig. 8F). No GXM polysaccharides were detected in the EVs released from the *ugg1*Δ, although the whole-cell extract of *ugg1*Δ mutant strain contained a significant quantity of GXM. Taken together with the reduced quantity of EV-associated proteins, the absence of GXM polysaccharides in the *ugg1*Δ EVs strongly indicates that EV cargo loading is defective when the ERQC is dysfunctional in *C. neoformans*.

Discussion

As glycoproteins pass through the secretory pathway, which starts at the ER, their *N*-linked glycans undergo extensive modifications in association with protein quality control. In mammals, the ERQC system is composed of ER glucosyltransferases (ALG6, ALG8, and ALG10), ER glucosidases (GLS1 and GLS2), ER chaperones (calnexin and calreticulin, CNX/CRT), and the folding sensor UGGT. The addition and removal of glucose residues enables the substrates to undergo cycles of binding and release, which promote accurate folding and prevent incompletely folded proteins from exiting the ER. After glucose trimming, α1,2-mannosidase I (ERManI) in the ER cleaves a mannose residue at the B branch of the M9 oligosaccharides and converts the core M9 *N*-glycans ($Man_9GlcNAc_2$) to M8 forms ($Man_8GlcNAc_2$). This step occurs before the accurately folded proteins are exported to the Golgi apparatus or misfolded proteins are redirected towards degradation (Fig. 1A, Ziegler et al., 1991, Herscovics, 2001). Thus, in most eukaryotes, $Man_8GlcNAc_2$ is the

final mature core *N*-glycan attached to glycoproteins in the ER before their transport to the Golgi complex for further *N*-glycan modification.

In contrast to higher eukaryotes, the ERQC system of *S. cerevisiae* is composed of glucosidase I, glucosidase II, and the calnexin Cne1 without a functional UGGT (Fig 1A; Supplementary Fig. 1A). Although Kre5 is homologous to UGGT, *S. cerevisiae* Kre5 functions are unrelated to the putative calnexin cycle in the ERQC, and the function of ER glucosidases I/II is primarily associated with the synthesis of cell wall β1,6-glucan (Fernandez et al., 1996; Simons et al., 1998). The ERQC composition of *C. neoformans* is unique in that it possesses UGGT but lacks the three glucosyltransferases necessary for adding glucose residues to the core precursor *N*-glycans (Park et al., 2012). This step is essential for generating the monoglucosylated form, which is recognized by CNE/CRT for initiating the folding mechanisms. Additionally, *C. neoformans* lacks CRT, which is the chaperone that aids CNE, and carries multiple α1,2-mannosidases. In this study, we investigated the molecular features and functions of the *N*-glycan-dependent ERQC in the human pathogen *C. neoformans*, which generates unique *N*-glycan precursors without glucose addition and shorter in length than those of most eukaryotes in the ER. Our data strongly suggest that despite the incomplete composition of the ERQC components, the UGGT-centered ERQC plays pivotal roles in cellular fitness, particularly in EV-mediated extracellular transport, which is crucial for pathogenicity.

The *C. neoformans ugg1*Δ mutant was avirulent in mice, a phenotype consistent with the observed defects in key virulence determinants, such as the polysaccharide capsule and melanin, as well as poor growth at 37 °C. The *mns1*Δ*101*Δ mutant displayed intermediate phenotypes between those of the WT and *ugg1*Δ. Our data from the UPR induction analysis and comparative transcriptomic analysis strongly indicate that the ERQC mutation generates ER stress; this accounts for significant similarity of the defective phenotypes of the *C.*

neoformans ERQC mutants to those reported in other mutants that exhibit defective protein folding in the ER, particularly in terms of increased stress sensitivity and decreased virulence. Connections between ER stress and thermotolerance have previously been established in *C. neoformans*, as growth at 37 °C requires key ER protein chaperones and protein processing machinery, including components of the UPR signaling pathway Ire1 and the ER stress-responsive transcription factor Hxl1 (Cheon et al., 2011; Havel et al., 2011; Jung et al., 2013). Other mutations causing defects in ER function in *C. neoformans*, such as mutants lacking *DNJ1* (an ER J-domain containing co-chaperone) and *CNE1* (an ER chaperone), resulted in growth inhibition. The *dnj1*Δ mutant strain displayed impaired elaboration of virulence factors, such as the exopolysaccharide capsule and extracellular urease activity, when cultured at human body temperature (Horianopoulos et al., 2021). Taken together with our data from the ERQC mutants, these findings strongly support the notion that maintaining ER homeostasis is crucial for survival and virulence factor production at elevated temperatures.

It is quite notable that the *C. neoformans ugg1*Δ EVs exhibited defective loading of GXM and many protein cargos, alongside a decrease in the number and changes in the size distribution of the extracellular EVs. Combined with compromised cell fitness, these defects in EV biogenesis and cargo loading, even under normal growth conditions, likely contribute to the complete loss of virulence owing to the defective export of virulence factors in the *ugg1*Δ mutant. EV generation involves complex molecular networks that function cooperatively or independently to mediate the invagination and fission of membranes and selective sorting of cargo molecules. Fungal EVs are produced and released under the maturation of endosomes into multivesicular bodies (MVBs). These MVBs are targeted to the cell surface, where they fuse with the plasma membrane and release luminal MVB vesicles into the outer space, serving as an unconventional secretion pathway (Oliveira et al., 2010). MVB formation requires the functionality of the endosomal sorting complex required for

transport (ESCR). The ESCRT pathway is highly complex and involves a series of finely regulated events (Henne et al., 2011). Deletion of several EV transport-related genes through the ESCRT complex directly impacts the cryptococcal capsule, primarily by reducing capsule size. Specifically, the *C. neoformans vps27*Δ strain, which is involved in the ESCRT complex, showed altered EV size distribution, reduced capsule dimensions, defects in laccase export to the cell wall, and poor extracellular export of urease (Park et al., 2020). Other regulators of unconventional secretion are also linked to EV biogenesis in *C. neoformans*. For example, the Golgi reassembly and stacking proteins (GRASPs) regulate EV cargo and dimensions (Peres et al., 2018). In *C. neoformans*, a *grasp*Δ mutant strain produced EVs with dimensions that significantly differed from those produced by WT cells, along with attenuated virulence and abnormal RNA composition. Moreover, the GRASP protein Grasp homology 1 (GRH1) serves as a chaperone that directly influences EV cargo (Malhotra, 2013; Peres da Silva et al., 2018). Autophagy regulators, which participate in EV formation in other eukaryotes, also play a role in cryptococcal EV formation. An *atg7*Δ strain manifests hypovirulence, and EVs produced by this strain show slightly different RNA composition compared with that of the WT cells (Oliveira et al., 2016).

It is intriguing how the absence of UGGT, leading to ERQC defects, results in defective EV biogenesis and cargo loading in *C. neoformans*. The ER is one of the largest organelles in the cell and is involved in multiple fundamental biological processes such as protein folding and secretion, Ca^{2+} storage, and lipid synthesis. In addition to protein folding, the ER is crucial for regulating lipid metabolism (Moncan et al., 2020). Several enzymes involved in triglyceride (TG) biosynthesis, cholesterol biosynthesis, and enzymes regulating membrane turnover and dynamics are located in the ER. Consequently, ER stress significantly impacts lipid and sterol synthesis, although some of these mechanisms are yet to be clarified. LDs aid the UPR and ERAD in degrading misfolded proteins during ER stress in

S. cerevisiae (Garcia et al., 2020). In the present study, we observed a drastic increase in LDs in the *ugg1*Δ mutant, consistent with the previous hypothesis that LDs help to maintain ER homeostasis. Furthermore, we observed increased number of vacuoles in *ugg1*Δ. The altered vesicular structures observed in the *ugg1*Δ and *mns1*Δ*101*Δ strains may indicate abnormal lipid homeostasis caused by the ERQC defects, which could, in turn, affect EV biogenesis. The importance of lipids and membrane regulators in proper EV formation and GXM export has been suggested in a previous study on the Apt1 flippase in *C. neoformans* (Rizzo et al., 2019). Additionally, ergosterol is essential for membrane fluidity, permeability, and protein transport (Ermakova and Zuev, 2017). Erg6 is an enzyme involved in the ergosterol biosynthesis pathway and was identified as essential for the trans-Golgi network transport of proteins (Proszynski et al., 2005; Nes et al., 2009). In *C. neoformans*, the *erg6*Δ mutant released EVs with a significantly larger diameter than those of the WT, carrying increased levels of proteins and sterols. This highlights the role of ergosterol in cryptococcal EV biogenesis (Oliveira et al., 2020). Taken together, these findings suggest that ER stress caused by misfolded glycoprotein accumulation in ERQC-defective mutants may alter lipid composition, which could affect EV biogenesis.

A recent study presented strong evidence for a key role of ER stress in modulating EV biogenesis by demonstrating that ER stress decreases exosome production through both adiponectin/T-cadherin-dependent and -independent pathways in mice (Fukuoka et al., 2023). They showed that T-cadherin is downregulated by ER stress through IRE1α activation at the mRNA and protein levels and that ER stress decreases EV production through adiponectin/T-cadherin-independent way, which might involve interferon pathway activation in mice. In this study, we similarly observed induced activity of Ire1 in *C. neoformans ugg1*Δ strain, even under normal culture conditions, which suggests a possible association between the Ire1-mediated UPR pathway and cryptococcal EV biogenesis (Fig. 9). Additionally, glycosylation

regulates the biogenesis of small EVs and affects protein cargo loading efficiency (Harada et al., 2020). This suggests that the altered *N*-glycosylation observed in *C. neoformans ugg1*Δ may influence cargo loading of certain EV-targeting glycoproteins. Future studies are needed to investigate the ERQC-mediated modulation of EV biogenesis and cargo loading in *C. neoformans*, as this will provide further insights into the mechanisms underlying the regulation, production, composition, and diversity of fungal EVs, which would enable a better understanding of their biological function. Expanding our knowledge on pathogenic fungal EVs would pave the way for utilizing native or engineered EVs as promising candidates for therapeutic applications, including fungal infection diagnosis and vaccine development.

Materials and Methods

Strains, culture conditions, plasmids, and primers

The *C. neoformans* strains that were constructed and used in this study are listed in Supplementary Table S1A. The plasmids and primers used are listed in Supplementary Tables S1B and S1C, respectively. The construction of the deletion mutants is described in the Supplementary Information. The strains were typically cultured in YPD medium (1% yeast extract, 2% bacto peptone, and 2% glucose) at 30 °C with shaking (220 rpm). *C. neoformans* transformants were selected by culturing on YPD solid medium containing 100 μg/ml nouseothricin acetyltransferase (Jena Bioscience, Germany; indicated as YPD_{NAT}), YPD solid medium with 100 μg/ml hygromycin B (Sigma-Aldrich, USA; indicated as YPD_{HyB}), or YPD solid medium with 100 μg/ml G418 (Duchefa, Netherlands; indicated as YPD_{NEO}). For capsule induction, *C. neoformans* cells were cultured in liquid Sabouraud dextrose medium (Difco) at 30 °C for 16 h and incubated in 10% Sabouraud dextrose medium (pH 7.3) supplemented with 50 mM morpholinepropanesulfonic acid (MOPS) at 30 °C for 2 days. For melanin production analysis, the cells were spotted onto an L-DOPA agar plate (7.6 mM L-asparagine monohydrate, 5.6 mM glucose, 22 mM KH_2PO_4, 1 mM $MgSO_4 \cdot 7H_2O$, 0.5 mM L-DOPA, 0.3 mM thiamine-HCl, and 20 nM biotin) and incubated at 30 °C or 37 °C for 2 days.

HPLC and MALDI-TOF-based *N*-glycan structure analysis

Cell wall mannoproteins (cwMPs) from *C. neoformans* were isolated and subjected to *N*-glycan structure analysis as described previously (Park et al., 2012; Thak et al., 2018). Briefly, *N*-glycans were released from purified cwMPs through PNGase F treatment (New England Biolabs, UK), followed by purification using a Carbograph Extract-Clean column. The purified *N*-glycans were labeled with 2-aminobenzoic acid (2-AA; Sigma-Aldrich, USA) and

further purified using a Cyano Base cartridge (Agilent, USA). 2-AA-labeled *N*-glycans were analyzed using a Waters 2690 HPLC system equipped with a 2475 fluorescence detector that was set to excitation and emission wavelengths of 360 nm and 425 nm, respectively. Data were collected using the Empower 2 software (Waters). For MALDI-TOF analysis, neutral *N*-glycans were collected from HPLC fractionation and dried. The matrix solution was prepared as previously described (Thak et al., 2018) and mixed with the samples in equal volumes. The samples were spotted on an MSP 96 polished-steek target (Bruker Daltonics, Germany), and the crystalized samples were analyzed using a Microflex mass spectrometer (Bruker Daltonics, Germany) in a linear negative mode.

Transmission electron microscopy

C. neoformans cells were cultured either at an initial optical density at 600 nm (OD_{600}) of 0.2 at 30 °C in YPD medium until OD_{600} reached 0.8 or for 2 days in 10% Sabouraud media at 30 °C. The cell pellets were washed twice in PBS and fixed for 12 h in 2% glutaraldehyde-2% paraformaldehyde in 0.1 M phosphate buffer (pH 7.4). The cells were washed in 0.1 M phosphate buffer and post-fixed with 1% OsO_4 in 0.1 M phosphate buffer for 2 h. The cells were dehydrated using an ascending ethanol series (50, 60, 70, 80, 90, 95, 100%) for 10 min each and infiltrated with propylene oxide for 10 min. The specimens were embedded with a Poly/Bed 812 kit (Polysciences Inc., USA) and polymerized in an electron microscope oven (TD-700, DOSAKA, Japan) at 65 °C for 12 h. The block was cut into 200-nm semi-thin sections with a diamond knife in the Ultramichrome and stained with toluidine blue for observation using optical microscopy. The region of interest was further cut into 80-nm thin sections using the ultramicrotome, placed on copper grids, double stained with 3% uranyl acetate for 30 min and 3% lead citrate for 7 min, and imaged using a transmission electron

microscope (JEM-1011, JEOL, Tokyo, Japan) equipped with a Megaview III CCD camera (Soft imaging system-Germany) at the acceleration voltage of 80 kV.

Animal study and *in vitro* survival analysis

Animal studies were conducted at the Chung-Ang University Animal Experiment Center. The study design was approved by the Ministry of Food and Drug Safety (MFDS, South Korea). Survival and fungal burden were assayed as described previously (Cheon et al., 2011). Briefly, eight mice (6-week-old female A/J Slc mice; Japan SLC) per strain were infected with 10^5 cells via intranasal instillation. The mice were weighed and monitored once daily and euthanized after rapid 30% weight loss or identification of signs of morbidity. Kaplan–Meier survival curves were generated using Prism version 7 (GraphPad Software). For performing the fungal burden assay, the lungs of *C. neoformans*-infected mice were dissected on days 7 or 60. Half-organ portions of the excised lungs were homogenized, serially diluted, and plated onto YPD medium containing 100 μg/ml chloramphenicol (Sigma-Aldrich, USA). The other half-lung samples were fixed, sectioned, and stained with mucicarmine (Abcam, UK) for histopathological analysis. *C. neoformans* colonization was analyzed using a Zeiss Axioscope (A1) equipped with an AxioCam MRm digital camera.

Cell survival within macrophages was analyzed by opsonizing *C. neoformans* cells with 10 mg/ml of 18B7 antibody at 37 °C for 1 h. The macrophage-like J774A.1 (10^5) cells were seeded onto 96-well plates in DMEM medium supplemented with 10% FBS and cultured at 37 °C in 5% CO_2 for 18 h. The opsonized *C. neoformans* (10^5) cells were co-incubated with activated macrophages at 37 °C in 5% CO_2 for 1 h. The non-phagocytized yeast cells were removed by washing each well thrice with PBS. Then, DMEM medium

supplemented with 10% FBS was added to each well, followed by culturing at 37 °C in 5% CO_2 for 24 h. The macrophages were lysed in distilled water by vigorous pipetting, and the fungal cells were collected and serially diluted. Cryptococcal survival was assessed using two independent colony forming unit (CFU) assays.

Capsule transfer and shedding analysis

Capsule transfer assays were performed as described previously (Reese and Doering, 2003). Briefly, conditioned medium (CM) was prepared as a source of GXM by culturing the respective strains for 5 days in YPD medium, followed by filtering and storing the culture supernatant at 4 °C. The acceptor strains were cultured overnight at 30 °C in YPD medium. In total, 2×10^6 acceptor cells were incubated with 1 µl of CM for 1 h at room temperature under rotation (18 rpm) and washed twice with PBS. Capsule acquisition was visualized by incubating the cells with an anti-GXM (18B7) antibody conjugated with AlexaFluor 488 (ThermoFisher Scientific, USA) for 1 h at 37 °C and observing under an Eclipse Ti-E fluorescence microscope (Nikon, Japan), equipped with a Nikon DS-Qi2 camera. The images were processed using the NIS-elements microscope imaging Software (Nikon, Japan). Capsule shedding analysis was performed by analyzing GXM shedding using a modified previously described protocol (Yoneda and Doering, 2008). The respective strains were cultured in 10% Sabouraud media for 2 days, and the culture supernatant was sterile filtered. Enzyme denaturation was performed by subjecting the filtrate to heating at 70 °C for 15 min, followed by centrifugation at 13,000 rpm for 3 min. Intracellular GXM analysis was performed by resuspending the pellets in TNE buffer (50 mM Tris-HCl [pH 7.5], 150 mM NaCl, 5 mM EDTA) with the same volume of glass beads (425–600 µm in diameter, Sigma-Aldrich, USA). The cells were disrupted four times for 15 s at 5,000 rpm using a Precellys 24

Tissue Homogenizer (Bertin Technologies, France), followed by centrifugation at 16,000 rpm for 5 min at 4 °C. Next, 10 µl of the supernatant of either secreted or intracellular polysaccharide was mixed with 6X loading dye and run on a 0.6% certified Megabase agarose (Bio-rad, USA) gel in 0.5X TBE (44.5 mM Trisma base, 44.5 mM boric acid, 1 mM EDTA [pH 8.0]) at 25 V for 16 h. The polysaccharides were transferred onto a nylon membrane using the southern blotting technique. The membrane was air-dried, blocked using 5% skim milk, and treated overnight with 2 µg/ml 18B7 antibody. After washing, the membrane was incubated with an anti-mouse peroxidase-conjugated secondary antibody and subjected to detection using chemiluminescence.

Detection of enzymatic activities in intracellular and secretary fractions

Biochemical enzymatic activities of acid phosphatase, urease, and laccase in the intracellular and secreted fractions were assayed spectrophotometrically, using previously described methods (Lev et al., 2014; Fu et al., 2018; de Sousa et al., 2022). Acid phosphatase activity was assayed by culturing cells in MM-KCL medium (0.5% KCl, 15 mM glucose, 10 mM $MgSO_4.7H_20$, 13 mM glycine, and 3 µM thiamine) for 3 h at 30 °C. The culture supernatant and soluble cell lysate were allowed to react with 2.5 mM p-nitrophenyl phosphate (pNPP) for 30 min at 37 °C. Urease activity was determined after culturing the cells in Rapid Urea broth (RUH) for 24 h at 30 °C and subjecting the culture supernatant and soluble cell lysate to incubation with phenol red. Laccase activity was assayed by culturing the cells in asparagine salts media (7.6 mM L-asparagine, 0.1% glucose, 22 mM KH_2PO_4, 1 mM $MgSO_4.7H_2O$, 0.3 mM thiamine-HCl, and 20 nM biotin) for 48 h at 30 °C and allowing the supernatant and soluble cell lysate to react overnight with 10 mM L-DOPA. The reactions were quantified by measuring OD_{420} (acid phosphatase), OD_{570} (urease), or OD_{480} (laccase).

Cellulase activity was determined by culturing the cells in cellulose media (0.1% $NaNO_3$, 0.1% K_2HPO_4, 0.1% KCl, 0.5% $MgSO_4$, 0.5% yeast extract, 0.1% glucose, and 0.5% low viscosity carboxymethyl cellulose) for 24 h at 30 °C. The culture supernatants were concentrated using an Amicon tube (30 kDa cutoff, Sigma-Aldrich, USA). The concentrated supernatants and soluble cell lysates were allowed to react at 40 °C for 10 min with the substrate 4,6-O-(3-ketobutylidene)-4-nitrophenyl-β-D-cellopentaoside (BPNPG5), which was provided in the cellulase assay kit (CellG5 Method, Megazyme, Ireland). The reaction was terminated by adding 2% [w/v] Tris buffer (pH 10), and the absorbance of 4-nitrophenol was measured at 400 nm. Cellulase activity (CellG5 Units/ml) was calculated as indicated in the cellulase assay kit. α-amylase activity was measured using the α-Amylase Activity Colorimetric Assay Kit (Biovision Technologies, USA) according to the manufacturer's instructions. Yeast cells were cultured overnight in YPD medium at 30 °C, and the culture supernatants were concentrated using an Amicon tube (30 kDa cutoff, Sigma-Aldrich, USA). The concentrated supernatants and soluble cell lysates were incubated for 1 h at 25 °C in assay buffer with the substrate ethylidene-pNP-G7, which was provided in the kit. OD_{405} was measured. All the activity analysis results were normalized according to cell density (OD_{600}).

Purification, nanoparticle tracking analysis (NTA), and Cryo-TEM imaging of extracellular vesicles

EV purification was performed according to a previously published protocol (Reis et al., 2019) with modifications. One loop of cells was inoculated into 10 ml of liquid YPD and incubated at 30 °C for 24 h with shaking (220 rpm). The cells were washed twice with 10 ml of PBS, counted, and diluted in PBS to a density of 3.5×10^7 cells/ml. Aliquots of cell suspension (300 μl) were spread onto synthetic dextrose (SD) solid medium plates and incubated for 24 h

at 30 °C. The cells were carefully recovered from each plate using an inoculation loop, gently resuspended in 30 ml PBS, and pelleted through centrifugation at 4,000 rpm for 10 min at 4 °C. The supernatant was collected and centrifuged again at 15,000 ×*g* for 15 min at 4 °C. Then, the supernatant was filtered through 0.45-μm syringe filters and ultracentrifuged at 100,000 ×*g* for 1 h at 4 °C (MLA-50 fixed angle rotor, Beckman Coulter, Germany). The supernatant was discarded, and the EV pellets were collected and resuspended in 1 ml of PBS for immediate use or stored at -80 °C for further experiments. The samples were diluted 100-fold, and EV sizes were measured using an NTA instrument (Nanosight Pro, Malvern Panalytical, Netherlands) coupled to a 532-nm laser (Malvern Panalytical, Netherlands), SCMOS camera (Hamamatsu Photonics. Japan), and syringe pump (Malvern Panalytical, Netherlands). The data were analyzed using the NS Xplorer software (v1.1.0.6, Malvern Panalytical, Netherlands).

Cryo-TEM imaging was performed by loading purified EVs (3 μl) onto a lacey carbon grid (Lacey Carbon, 300mesh Cu, Ted Pella Inc., USA), which was glow discharged at 15 mA for 60 s. The sample-loaded grid was blotted for 3 s at 15 °C and 100% humidity and immediately plunge-frozen in liquid ethane. The process was performed by Vitrobot Maek IV (Thermofisher Scientific, USA, SNU, CMCI). The frozen grids were imaged using TEM (JEM-2100F, JEOL, Japan); the temperature of the grid was maintained at approximately -180 °C at an acceleration voltage of 200 keV. The images were recorded using an ultrascan 1000 electron detector.

EV proteome analysis

EVs proteins were solubilized in 8 M urea, 100 mM Tris (pH 7.5), and 5 mM tris (2-

carboxyethyl) phosphine (TCEP) for 20 min at 23 °C. The protein concentration was quantified using the Protein Assay Dye (Bio-rad, USA). A Protifi S-TrapTM mini spin column (C02-mini-80, Protifi, USA) was used to process each sample. After digesting with trypsin gold (V5280, Promega, USA), the digested peptides were eluted using 50 mM tetraethylammonium bromide (TEAB; Thermo Fisher Scientific, USA), 0.2% formic acid, and 50% acetonitrile. The pooled peptide solution was dried, dissolved in 100 mM TEAB, and labeled using TMTpro™ 16plex Label Reagent Set (Thermo Fisher Scientific, USA). The labeled peptides (total, 100 µg proteins) were combined prior to offline basic reverse-phase liquid chromatographic (bRPLC) fractionation. Linear gradient was performed using buffer A (10 mM TEAB in water) and buffer B (10 mM TEAB in 90% acetonitrile), and 10 fractions were analyzed in total using am LC-MS/MS system. The samples were dissolved in 0.1% formic acid using an UltiMate 3000 RSLCnano system and analyzed using an Orbitrap Eclipse Tribrid mass spectrometer (Thermo Fisher Scientific, USA). All MS raw files were converted into mzML and ms2 file formats using the MSConvert (version 3.0.20033) software.

The *C. neoformans* proteome was determined by downloading a protein FASTA file from Uniprot (http://uniprot.org), which included 30,647 reviewed (Swiss-Prot) and unreviewed (TrEMBL) proteins entries. A proteome search database with reversed sequence and contaminants in the Integrated Proteomics Pipeline (IP2, version 5.1.2, Integrated Proteomics Applications Inc., San Diego, CA) was generated. The proteome search from 20 ms2 files was performed with IP2 and its following parameters, followed by evaluation for a false discovery rate (FDR) using IP2 and Proteininferencer (version 1.0, Integrated Proteomics Applications Inc., USA). Protein quantification and statistical analysis for discovery of differentially expressed proteins (DEPs) was performed using the ms2 files with

tandem mass tag (TMT) reporter ions using an in-house program coded using Python 3.8, where t-test and Pearson's correlation analysis between comparison samples was performed using the scikit-learn (version 0.23.2), Scipy (version 1.6.0), and statsmodels (0.12.1) Python libraries.

Acknowledgments

We thank Arturo Casadevall for providing the 18B7 antibody, Jennifer K. Lodge for providing the anti-Cda1 antibody, and Ji-Yeon Kang for technical assistance with MALDI-TOF analysis.

Competing Interests

The authors declare no conflicts of interest.

Additional information

Funding

This study was supported by the National Research Foundation of Korea (Grant nos. NRF-2022R1A2C1012699, NRF2018R1A5A1025077, and RS-2023-00212663) and by the Korea Institute of Marine Science & Technology Promotion (Grant no. RS-2024-00405273).

Author Contributions

Catia Mota: Investigation, Construction of mutants, Performing all virulence analysis, Data curation, and Writing—original draft; Kiseung Kim: Construction of mutants and Performing phenotype analysis; Ye Ji Son: Transcriptome analysis and Validation; Eun Jung Thak and Su-Bin Lee: Glycan analysis; Ju-El Kim and Jeong-Kee Yoon: NTA analysis; Min-Ho Kang: Cryo-TEM analysis; Heeyoun Hwang: Proteome analysis; Yong-Sun Bahn and J. Andrew Alspaugh: Supervision, Data curation, Writing—review, and editing; Hyun Ah Kang: Conceptualization, Project administration, Supervision, Data curation, Writing—original draft, review, and editing.

Author ORCIDs

Catia Mota: orcid.org/0009-0001-6129-0000

Ye Ji Son: orcid.org/0009-0006-4324-5800

Eun Jung Thak: orcid.org/0000-0003-4523-142X

Ju-El Kim: orcid.org/0009-0002-3028-1125

Jeong-Kee Yoon: orcid.org/0000-0003-0111-9911

Heeyoun Hwang: orcid.org/0000-0002-0124-2533

Yong-Sun Bahn: orcid.org/0000-0001-9573-5752

J. Andrew Alspaugh: orcid.org/0000-0003-3009-627X

Hyun Ah Kang: orcid.org/0000-0002-3722-525X

Additional files

Supplementary files

Supplementary file 1 – Supplementary material & methods. (a) Construction of *C.*

*neoformans ugg1*Δ and *UGG1* complementation strains. (b) Construction of *C. neoformans mns1*Δ, *mns101*Δ, *mns1*Δ*101*Δ, and respective complementation strains. (c) Construction of *C. neoformans mnl1*Δ, *mnl2*Δ and, *mnl1*Δ*mnl2*Δ strains. (d) Construction and localization analysis of *C. neoformans* GFP-Ugg1, Mns1-GFP, and Mns101-GFP fusion proteins. (e) Localization analysis of *C. neoformans* GFP-Ugg1, Mns1-GFP, and Mns101-GFP. (f) Partial fractionation and western blotting analysis of Cda1. (g) RNA preparation, qRT-PCR, and RNA-sequencing.

Supplementary file 2 - Supplementary figures. (a) Figure S1. Evolutionary conservation and divergence of endoplasmic reticulum quality control (ERQC)-related gene homologues predicted in different eukaryote organisms. (b) Figure S2. Domain analysis of putative *C. neoformans* ERQC-associated proteins. (c) Figure S3. Phenotype characterization of *C. neoformans mnl1*Δ, *mnl2*Δ, and *mnl1*Δ*mnl2*Δ. (d) Figure S4. Fungal burden of mice infected with *C. neoformans* ERQC-related mutant cells. (e) Figure S5. Lipid and vacuole staining of the wild type (WT) and *ugg1*Δ strains. (f) Figure S6. Comparative analysis of extracellular vesicles (EV) proteomes between WT and *ugg1*Δ.

Supplementary file 3 - Table S1. A. List of strains used in this study; B. List of plasmids used in this study; C. List of primers used in this study.

Supplementary file 4 - Table S2. A. Up-regulated (> 2-fold) *Cryptococcus neoformans* genes in *ugg1*Δ than that of wild type (WT) cultivated in yeast extract peptone dextrose (YPD) at 30 °C, B. Down-regulated (> 2-fold) *Cryptococcus neoformans* genes in *ugg1*Δ than that of wild type (WT) cultivated in YPD at 30 °C.

Supplementary file 5 - Table S3. List of proteins identified using proteomic analysis in wild type (WT) and *ugg1*Δ extracellular vesicles (EVs).

Supplementary file 6 - Table S4. Representative extracellular vesicle (EV)-associated proteins commonly detected in this study and previously reported *Cryptococcus neoformans* EV proteome data sets.

Data availability

The raw RNA sequencing data have been submitted to the NCBI GEO database under accession no. GSE254772.

References

Aebi M. 2013. *N*-linked protein glycosylation in the ER. *Biochim Biophys Acta*. **1833**: 2430-2437.

Almeida F, Wolf JM, Casadevall A. 2015. Virulence-associated enzymes of *Cryptococcus neoformans*. *Eukaryot Cell* **14**: 1173-1185.

Balchin D, Hayer-Hartl M, Hartl FU. 2016. In vivo aspects of protein folding and quality control. *Science* **353**: aac4354.

Baker LG, Specht CA, Donlin MJ, Lodge JK. 2007. Chitosan, the deacetylated form of chitin, is necessary for cell wall integrity in *Cryptococcus neoformans*. *Eukaryot Cell* **6**: 855-867.

Baker LG, Specht CA, Lodge JK. 2011. Cell wall chitosan is necessary for virulence in the opportunistic pathogen *Cryptococcus neoformans*. *Eukaryot Cell* **10**: 1264-1268.

Banerjee S, Vishwanath P, Cui J, Kelleher DJ, Gilmore R, Robbins PW, Samuelson J**.** 2007. The evolution of *N*-glycan-dependent endoplasmic reticulum quality control factors for glycoprotein folding and degradation. *Proc Natl Acad Sci USA* **104**: 11676-11681.

Bleackley MR, Dawson CS, Anderson MA. 2021. Fungal extracellular vesicles with a focus on proteomic analysis. *Proteomics* **19**: e1800232.

Casadevall A, Coelho C, Cordero RJB, Dragotakes Q, Jung E, Vij R, Wear MP**.** 2019. The capsule of *Cryptococcus neoformans*. *Virulence* **10**: 822-831.

Cheon SA, Jung KW, Chen YL, Heitman J, Bahn YS, Kang HA**.** 2011. Unique evolution of the UPR pathway with a novel bZIP transcription factor, Hxl1, for controlling pathogenicity of *Cryptococcus neoformans*. *PLoS Pathog* **7**: e1002177.

Collopy-Junior I, Esteves FF, Nimrichter L, Rodrigues ML, Alviano CS, Meyer-Fernandes JR. 2006. An ectophosphatase activity in *Cryptococcus neoformans*. *FEMS Yeast Research* **6**: 1010–1017.

de Sousa HR, de Oliveira GP Jr, Frazão SO, Gorgonha KCM, Rosa CP, Garcez EM, Lucas J Jr, Correia AF, de Freitas WF, Borges HM, Brito Alves LG, Paes HC, Trilles L, Lazera MDS, Teixeira MM, Pinto VL Jr, Felipe MSS, Casadevall A, Silva-Pereira I, Albuquerque P, Nicola AM. 2022. Faster *Cryptococcus* melanization increases virulence in experimental and human cryptococcosis. *J Fungi* **8**: 393.

Doering TL. 2009. How sweet it is! Cell wall biogenesis and polysaccharide capsule formation in *Cryptococcus neoformans*. *Annu. Rev. Microbiol* **63**: 223-247.

Ermakove E, Zuev Y. 2017. Effect of ergosterol on the fungal membrane properties. All atom and coarse-grained molecular dynamics study. *Chem. Phys. Lipids* **209**: 45-53.

Fu MS, Coelho C, De Leon-Rodriguez CM, Rossi DCP, Camacho E, Jung EH, Kulkarni M, Casadevall A. 2018. *Cryptococcus neoformans* urease affects the outcome of intracellular pathogenesis by modulating phagolysosomal pH. *PLoS Pathog* **14**: e1007144.

Fukuoka K, Mineo R, Kita S, Fukuda S, Okita T, Kawada-Horitani E, Iioka M, Fujii K, Kawada K, Fukushima Y, Nishizawa H, Maeda N, Shimomura L. 2023, ER stress decreases exosome production through adiponectin/T-cadherin-dependent and -independent pathways. *J Biol Chem* **299**: 105-114.

Garcia EJ, Liao PC, Tan G, Vevea JD, Sing CN, Tsang CA, McCaffery JM, Boldogh IR, Pon LA. 2021. Membrane dynamics and protein targets of lipid droplet microautophagy during ER stress-induced proteostasis in the budding yeast, *Saccharomyces cerevisiae*. *Autophagy* **17**: 2363-2383.

Garcia-Rivera J, Chang YC, Kwon-Chung KJ, Casadevall A. 2004. *Cryptococcus neoformans* CAP59 (or Cap59p) is involved in the extracellular trafficking of glucuronoxylomannan. *Eukaryot Cell* **3**: 385-392.

Grijpstra J, Tefsen B, van Die I, de Cock H. 2009. The *Cryptococcus neoformans* cap10 and cap59 mutant strains, affected in glucuronoxylomannan synthesis, differentially activate human dendritic cells. *FEMS Immunol Med Microbiol* **57**: 142-150.

Gottfredsson M, Perfect JR. 2000. Fungal Meningitis. *Semin. Neurol* **20**: 307-322.

Harada Y, Nakajima K, Suzuki T, Fukushige T, Kondo K, Seino J, Ohkawa Y, Suzuki T, Inoue H, Kanekuta T, Dohmae N, Taniguchi N, Maruyama I. 2020. Glycometabolic regulation of the biogenesis of small extracellular vesicles. *Cell Rep* **33**: 108261.

Havel VE, Wool NK, Ayad D, Downey KM, Wilson CF, Larsen P, Djordjevic JT, Panepinto JC. 2011. Ccr4 promotes resolution of the endoplasmic reticulum stress response during host temperature adaptation in *Cryptococcus neoformans. Eukaryot Cell* **10**: 895–901.

Henne WM, Buchkovich NJ, Emr SD. 2011. The ESCRT pathway. *Dev Cell* **21**: 77-91.

Herscovics A. 2001. Structure and function of Class I alpha 1,2-mannosidases involved in glycoprotein synthesis and endoplasmic reticulum quality control. *Biochimie* **83**: 757-762.

Horianopoulos LC, Lee CWJ, Hu G, Caza M, Kronstad JW. 2021. Dnj1 promotes virulence in *Cryptococcus neoformans* by maintaining robust endoplasmic reticulum homeostasis under temperature stress. *Front Microbiol* **12**: 727039.

Jung KW, Kang HA, Bahn YS. 2013. Essential roles of the Kar2/BiP molecular chaperone downstream of the UPR pathway in *Cryptococcus neoformans*. *PLoS One* **8**: e58956.

Kwon-Chung KJ, Sorrel TC, Dromer F, Fung E, Levitz SM. 2000. Cryptococcosis: clinical and biological aspects. *Med. Mycol* **38**: 205-213

Lee SB, Mota C, Thak EJ, Kim J, Son YJ, Oh DB, Kang HA. 2023. Effects of altered *N*-glycan structures of *Cryptococcus neoformans* mannoproteins, MP98 (Cda2) and MP84 (Cda3), on interaction with host cells. *Sci Rep* **13**: 1175.

Lev S, Crossett B, Cha SY, Desmarini D, Li C, Chayakulkeeree M, Wilson CF, Williamson PR, Sorrel TC, Djordjevic JT. 2014. Identification of Aph1, a phosphate-regulated, secreted, and vacuolar acid phosphatase in *Cryptococcus neoformans*. *mBio* **5**: e01649-14.

Malhotra V. 2013. Unconventional protein secretion: an evolving mechanism. *EMBO J* **32**: 1660-1664.

Moncan M, Mnich K, Blomme A, Almanza A, Samali A, Gorman AM. 2021. Regulation of lipid metabolism by the unfolded protein response. *J Cell Mol Med*. **25**: 1359-1370.

Nes WD, Zhou W, Ganapathy K, Liu JL, Vatsyayan R, Chamala S, Hernandez K, Miranda M. 2009. Sterol 24-C-methyltransferase: An enzymatic target for the disruption of ergosterol biosynthesis and homeostasis in *Cryptococcus neoformans*. *Arch. Biochem. Biophys* **481**: 210-218.

Olszewski MA, Noverr MC, Chen GH, Toews GB, Cox GM, Perfect JR, Huffnagle GB. 2004. Urease expression by *Cryptococcus neoformans* promotes microvascular sequestration, thereby enhancing central nervous system invasion. *Am J Pathol* **164**: 1761-1771.

Oliveira DL, Nakayasu ES, Joffe LS, Guimarães AJ, Sobreira TJP, Nosanchuk JD, Cordero RJB, Frases S, Casadevall A, Almeida IC, Nimrichter L, Rodrigues ML. 2010. Characterization of yeast extracellular vesicles: evidence for the participation of different pathways of cellular traffic in vesicle biogenesis. *PLoS ONE* **5**: e11113.

Oliveira DL, Fonseca FL, Zamith-Miranda D, Nimrichter L, Rodrigues J, Pereira MD, Reuwsaar JC, Schrank A, Staats C, Kmetzsch L, Vainstein MH, Rodrigues ML. 2016. The putative autophagy regulator Atg7 affects the physiology and pathogenic mechanisms of *Cryptococcus neoformans*. *Future Microbiol* **11**: 1405-1419.

Oliveira FFM, Paes HC, Peconick LDF, Fonseca FL, Marina CLF, Bocca AL, Homem-de-Mello M, Rodrigues ML, Albuquerque P, Nicola AM, Alspaugh JA, Felipe MSS, Fernandes L. 2020. Erg6 affects membrane composition and virulence of the human fungal pathogen *Cryptococcus neoformans*. *Fungal Genet. Biol* **140**: e103368.

O'Meara TR, Norton D, Price MS, Hay C, Clements MF, Nichols CB, Alspaugh JA. 2010. Interaction of *Cryptococcus neoformans* Rim101 and protein kinase A regulates capsule. *PLoS Pathogens* **6**: e1000776.

Park JN, Lee DJ, Kwon O, Oh DB, Bahn YS, Kang HA. 2012. Unraveling unique structure and biosynthesis pathway of *N*-linked glycans in human fungal pathogen *Cryptococcus neoformans* by glycomics analysis. *J Biol Chem* **287**: 19501–19515.

Park YD, Chen SH, Camacho E, Casadevall A, Williamson PR. 2020. Role of the ESCRT pathway in laccase trafficking and virulence of *Cryptococcus neoformans*. *Infect Immun* **88**: e00954-19.

Peres da Silva R, Martins SDT, Rizzo J, Dos Reis FCG, Joffe LS, Vainstein M, Kmetzsch L, Oliveira DL, Puccia R, Goldenberg S, Rodrigues ML, Alves LR. 2018. Golgi reassembly and stacking protein (GRASP) participates in vesicle-mediated RNA export in *Cryptococcus neoformans*. *Genes* **9**: 400.

Ploegh HL. 2007. A lipid-based model for the creation of an escape hatch from the endoplasmic reticulum. *Nature* **448**: 435–438.

Proszynski TJ, Klemm RW, Gravert M, Hsu PP, Gloor Y, Wagner J, Kozak K, Grabner H, Walzer K, Bagnat M, Simons K, Walch-Solimena C. 2005. A genome-wide visual screen reveals a role for sphingolipids and ergosterol in cell surface delivery in yeast. *Proc. Natl. Acad. Scie. U.S.A* **102**: 32201128.

Qiu Y, Davis M.J, Dayrit JK, Hadd Z, Meister DL, Osterholzer JJ, Williamson PR, Olszewski MA. 2012. Immune modulation mediated by cryptococcal laccase promotes pulmonary growth and brain dissemination of virulent *Cryptococcus neoformans* in mice. *PLoS ONE* **7**: e47853.

Rapoport TA. 2007. Protein translocation across the eukaryotic endoplasmic reticulum and bacterial plasma membranes. *Nature* **450**: 663-669.

Reis FCG, Borges BS, Jozefowicz LJ, Sena BAG, Garcia AWA, Medeiros LC, Martins ST, Honorato L, Schrank A, Vainstein MH, Kmetzsch L, Nimrichter L, Alves LR, Staats CC, Rodrigues ML. 2019. A novel protocol for the isolation of fungal extracellular vesicles reveals the participation of a putative scramblase in polysaccharide export and capsule construction in *Cryptococcus gattii*. *mSphere* **4**: e00080-19.

Rizzo J, Wong SSW, Gazi AD, Moyrand F, Chaze T, Commere PH, Novault S, Matondo M, Péhau-Arnaudet G, Reis FCG, Vos M, Alves LR, May RC, Nimrichter L, Rodrigues ML, Aimanianda V, Janbon G. 2021. *Cryptococcus* extracellular vesicles properties and their use as vaccine platforms. *J Extracell Vesicles* **10**: e12129.

Rizzo J, Colombo AC, Zamith-Miranda D, Silva VKA, Allegood JC, Casadevall A, Del Poeta M, Nosanchuk JD, Kronstad JW, Rodrigues ML. 2018. The putative flippase Apt1 is required for intracellular membrane architecture and biosynthesis of polysaccharide and lipids in *Cryptococcus neoformans*. *Biochim Biophys Acta Mol Cell Res* **1865**: 532-541.

Reese AJ, Doering TL. 2003. Cell wall alpha-1,3-glucan is required to anchor

the *Cryptococcus neoformans* capsule. *Mol. Microbiol.* **50**: 1401–1409.

Rodrigues ML, Nimrichter L, Oliveira DL, Frases S, Miranda K, Zaragoza O, Alvarez M, Nakouzi A, Feldmesser M, Casadevall A. 2007. Vesicular polysaccharide export in *Cryptococcus neoformans* is a eukaryotic solution to the problem of fungal trans□cell wall transport. *Eukaryotic Cell* **6**: 48–59.

Rodrigues ML, Nakayasu ES, Oliveira DL, Nimrichter L, Nosanchuk JD, Almeida IC, Casadevall A. 2008. Extracellular vesicles produced by *Cryptococcus neoformans* contain protein components associated with virulence. *Eukaryotic Cell* **7**: 58–67.

Samuelson J, Banerjee S, Magnelli P, Cui J, Kelleher DJ, Gilmore R, Robbins PW. 2005. The diversity of dolichol-linked precursors to Asn-linked glycans likely results from secondary loss of sets of glycosyltransferases. *Proc Natl Acad Sci USA* **102**: 1548-1553.

Samuelson J, Robbins PW. 2015. Effects of *N*-glycan precursor length diversity on quality control of protein folding and on protein glycosylation. *Semin Cell Dev Biol.* **41**: 121-128.

Singh A, Panting RJ, Varma A, Saijo T, Waldron KJ, Jong A, Ngamskulrungroj P, Chang YC, Rutherford JC, Kwon-Chung KJ. 2013. Factors required for activation of urease as a virulence determinant in *Cryptococcus neoformans*. *mBio* **4**: e00220-13.

Specht CA, Lee CK, Huang H, Hester MM, Liu J, Luckie BA, Santana MAT, Mirza Z, Khoshkenar P, Abraham A, Shen Zu T, Lodge JK, Akalin A, Homan J, Ostroff GR, Levitz SM. 2017. Vaccination with recombinant *cryptococcus* proteins in glucan particles protects mice against cryptococcosis in a manner dependent upon mouse strain and cryptococcal species. *mBio* **8**: e01872–17.

Thak EJ, Kim J, Lee DJ, Kim JY, Kang HA. 2018. Structural analysis of *N*-/*O*-glycans assembled on proteins in yeasts. *J Microbiol* **56**: 11–23.

Thak EJ, Lee SB, Xu-Vanpala S, Lee DJ, Chung SY, Bahn YS, Oh DB, Shinohara ML, Kang HA. 2020. Core *N*-glycan structures are critical for the pathogenicity of *Cryptococcus neoformans* by modulating host cell death. *mBio* **11**: e00711-00720.

Thak EJ, Son YJ, Lee DJ, Kim H, Kim JH, Lee SB, Jang YB, Bahn YS, Nichols CB, Alspaugh JA, Kang HA. 2022. Extension of *O*-linked mannosylation in the Golgi apparatus is critical for cell wall integrity signaling and interaction with host cells in Cryptococcus neoformans pathogenesis. mBio **13**: e0211222.

Thibault G, Ng DT. 2012. The endoplasmic reticulum-associated degradation pathways of budding yeast. *Cold Spring Harb Perspect Biol.* **4**: a013193.

Upadhya R, Lam WC, Hole CR, Parchment D, Lee CK, Specht CA, Levitz SM, Lodge JK. 2021. *Cryptococcus neoformans* Cda1 and Cda2 coordinate deacetylation of chitin during infection to control fungal virulence. *Cell Surf* **7**: 100066.

Varki A. (2017) Biological roles of glycans. *Glycobiology*. **27**:3-49.

Vevea JD, Garcia EJ, Chan RB, Zhou B, Schultz M, Di Paolo G, McCaffery JM, Pon LA. 2015. Role for lipid droplet biogenesis and microlipophagy in adaptation to lipid imbalance in yeast. *Dev Cell* **35**: 584–599.

Wolf JM, Espadas-Moreno J, Luque-Garcia JL, Casadevall A. 2014. Interaction of *Cryptococcus neoformans* extracellular vesicles with the cell wall. *Eukaryot Cell* **13**: 1484-1493.

Yoneda A, Doering TL. 2006. A eukaryotic capsular polysaccharide is synthesized intracellularly and secreted via exocytosis. *Mol Biol Cell* **17**: 5131–5140.

Yoneda A, Doering TL. 2008. Regulation of *Cryptococcus neoformans* capsule size is mediated at the polymer level. *Eukaryotic Cell* **7**: 546–549.

Xu C, Ng DT. 2015. Glycosylation-directed quality control of protein folding. *Nat Rev Mol Cell Biol* **16**: 742-752.

Zaragoza O, Rodrigues ML, De Jesus M, Frases S, Dadachova E, Casadevall A. 2009. The capsule of the fungal pathogen *Cryptococcus neoformans*. *Adv. Appl. Microbiol* **68**: 133–216.

Ziegler FD, Trimble RB. 1991. Glycoprotein biosynthesis in yeast: purification and characterization of the endoplasmic reticulum Man_9 processing α-mannosidase. *Glycobiology* **1**: 605-614.

Zhu X, Williamson PR. 2004. Role of laccase in the biology and virulence of *Cryptococcus neoformans*. *FEMS Yeast Res*. **5**: 1–10.

Figure legends

Figure 1. **Presence of UDP-glucose:glycoprotein glucosyltransferase (UGGT) and α1,2-mannosidases as endoplasmic reticulum protein quality control (ERQC) components in *Cryptococcus neoformans*.** (A) Graphical representation of the ERQC pathway in *Hommo sapiens*, *Saccharomyces cerevisiae*, and *Cryptococcus neoformans*. (B) Domain structures of proteins encoded by *C. neoformans UGG1* (CNAG_03648), *MNS1* (CNAG_02081), *MNS101* (CNAG_03240), *MNL1* (CNAG_01987), and *MNL2* (CNAG_04498). (C). Induced expression of ERQC genes in *C. neoformans*. Yeast cells were cultured in yeast extract peptone dextrose (YPD) medium to a mid-logarithmic phase and exposed to dithiothreitol (DTT; 20 mM). Tunicamycin (TM; 5 μg/ml) or to 37 °C for 1 h. The relative transcript levels of *C. neoformans* genes were analyzed using qRT-PCR. Transcript levels were normalized with that of *ACT1*. Error bars represent standard deviation of duplicated assays. All statistical data were determined based on one-way ANOVA and Dunnett's post-hoc test. *** $P < 0.0005$, ** $P < 0.003$, *** $P < 0.005$, * $P < 0.05$.

Figure 2. High performance liquid chromatography (HPLC)-based *N*-glycan profiles of *C. neoformans* ERQC mutant strains (A) Analysis of *N*-glycan profiles of the *ugg1*Δ mutant. (B) Silver staining and lectin blotting of sodium dodecyl sulphate (SDS)-polyacrylamide gels containing intracellular or secreted proteins into the culture supernatants of the wild type (WT) and *ugg1*Δ strains. Yeast cells were cultivated in YPD medium for 24 h, harvested, and subjected to sample preparation of soluble intracellular proteins and secreted proteins. The samples (30 μg, proteins) were loaded on 15% SDS-polyacrylamide gel and analyzed using silver staining (left) or blotting (right) with *Galanthus nivalis* agglutinin (Roche), which recognizes terminal α1,2-, α1,3-, and α1,6-linked mannose residues. (C)

HPLC analysis of total *N*-glycan profiles of *mns1*Δ, *mns101*Δ, and *mns1*Δ*101*Δ mutants. (D) MALDI-TOF profiles of neutral *N*-glycans of *mns1*Δ, *mns101*Δ, and *mns1*Δ*101*Δ mutants. The *N*-glycans of cell wall mannoproteins from WT, *ugg1*Δ, *ugg1*Δ::*UGG1*, *mns1*Δ, *mns101*Δ, *mns1*Δ*101*Δ, *mns1*Δ*::MNS1*, *mns1*Δ*::MNS101*, *mns1*Δ*101*Δ*::MNS1*, and *mns1*Δ*101*Δ*::MNS101* mutant strains were AA-labelled and analyzed using HPLC. Neutral *N*-glycan fractions were obtained from the HPLC fractionation of total *N*-glycans.

Figure 3. Growth phenotype of *C. neoformans* ERQC mutant strains Spotting analysis of *C. neoformans ugg1*Δ (A) and *mns1*Δ*101*Δ (B) mutant strains under various stress conditions such as heat stress (37 °C and 39 °C), ER stress (DTT: dithiothreitol, TM: tunicamycin), cell-wall stress (CFW: calcofluor white, CR: Congo red, SDS: Sodium dodecyl sulfate, caffeine), osmotic stress (NaCl, KCl, sorbitol) and treatment with antifungal drugs (fluconazole, ketoconazole, fludioxonil). (C) Growth analysis in the presence of 5',5',5'-trifluoroleucine (TFL). Respective strains were spotted on SC-Leucine media with or without TFL supplementation. Plates were incubated for 3 days at 30 °C. (D) RT-PCR analysis of *IRE1*-dependent splicing of *HXL1*. Strains were cultured in YPD supplemented with 5 μg/ml tunicamycin (TM). (E) Subcellular localization of GFP-tagged Ugg1, Mns1, and Mns101. ER tracker was used to visualize the ER membrane. Scale bar, 2.5 μm.

Figure 4. *In vitro* and *in vivo* virulence-associated phenotypes of *C. neoformans UGG1, MNS1,* and *MNS101* mutant strains (A, B) Melanin synthesis. WT, *ugg1*Δ, *ugg1*Δ*::UGG1*, *mns1*Δ, *mns101*Δ, *mns1*Δ*101*Δ, *mns1*Δ*101*Δ*::MNS1*, *mns1*Δ*101*Δ*::MNS101*, and *cac1*Δ (negative control) strains were serially diluted, plated on L-DOPA plates, and incubated at

30 °C and 37 °C. (C) Capsule formation. Cells were cultured for 2 days in 10% Sabouraud media at 30 °C and observed under the microscope. Statistical significance: ****, $P < 0.0001$, ns, not significant.). (D) *In vivo* virulence analysis. A/Jcr mice (n=8) were infected with 10^5 cells of WT, *ugg1*Δ, and *ugg1*Δ*::UGG1*, *mns1*Δ, *mns101*Δ, *mns1*Δ*101*Δ, *mns1*Δ*101*Δ*::MNS1*, and *mns1*Δ*101*Δ*::MNS101* strains, and survival was monitored for 2 months. (E) Survival of *C. neoformans* in macrophages. Survival of *C. neoformans* cells within the J774A.1 macrophage-like cell line was determined by counting colony formation unit (CFU) obtained from lysed macrophages from two biologically independent experiment sets. **** $P < 0.0001$, *** $P < 0.0005$, * $P < 0.05$, ns, not significant. All statistical data were determined based on one-way ANOVA and Dunnett's post-hoc test.

Figure 5. Capsule shedding and transfer analysis of *C. neoformans UGG1, MNS1*, and *MNS101* mutant strains (A) Capsule shedding analysis. Presence of intracellular (left) and shed (right) glucuronoxylomannan (GXM) was assessed by blotting a cell culture filtrate using the monoclonal antibody 18B7. The arrow indicates the direction of electrophoresis. (B) Capsule transfer analysis using exogenous capsule material from WT. The capsule transfer assay was performed using the indicated strains as acceptors. Surface capsules were probed using the anti-GXM antibody 18B7 conjugated with AlexaFluor 488. Quantitative measurement of fluorescence intensity was calculated based on two independent triplicate experiments with standard deviations presented as error bars. (C) Capsule transfer analysis using exogenous capsule material from WT or *mns1*Δ*101*Δ. Statistical significance: **** $P < 0.0001$. All statistical data were determined based on one-way ANOVA and Dunnett's post-hoc test. (D) Transmission electron microscopy (TEM) of *C. neoformans* WT, *ugg1*Δ, and *mns1*Δ*101*Δ strains. Yeast cells were grown overnight at 30 °C in YPD medium and fixed in 2%

glutaraldehyde and 2% paraformaldehyde. A Zeiss Axioscope (A1) equipped with an AxioCan MRm digital camera was used to visualize India ink-stained *C. neoformans* cells. Specimens were prepared using critical point drying prior to TEM microscopy. Capsule and yeast cell body diameters were measured using ImageJ (National Institute of Health).

Figure 6. Transcriptome analysis of *C. neoformans* WT and *ugg1*Δ cells (A) Volcano plot comparing a 2-fold differential gene expression between *ugg1*Δ and WT strains under normal growth conditions. (B) Number of genes upregulated and downregulated by ≥ 2-fold in *ugg1*Δ compared with that of the WT. (C) Gene ontology (GO) analysis of differentially expressed genes between WT and *ugg1*Δ strains. Significantly upregulated genes in *ugg1*Δ are shown in red, whereas significantly downregulated genes in *ugg1*Δ are shown in blue. Total RNA was extracted and subjected to RNAseq analysis as described in the Supplementary Information. (D) qRT-PCR analysis of mRNA expression levels of a set of genes responsible for capsule biosynthesis, cell wall remodeling, and both conventional and non-conventional secretion in *ugg1*Δ vs WT under normal growth conditions from three biologically independent experiment sets.

Figure 7. Analysis of protein secretion in *C. neoformans UGG1*, *MNS1*, and *MNS101* mutant strains (A) Spot assay for urease analysis on Christensen's urea agar. Absence of pink coloration indicates loss of urease activity. (B, C, D) Analysis of secretion for virulence-related enzymes such as urease, laccase, and acid phosphatase from three biologically independent experiment sets. Statistical significance: **** $P < 0.0001$, ** $P < 0.003$, *** $P < 0.005$, * $P < 0.05$. All statistical data were determined based on one-way ANOVA and

Dunnett's post-hoc test. (E, F) Analysis of secretion for non-virulence-related enzymes such as cellulase and α-amylase. Statistical significance: *** $P<0.0005$, ** $P<0.003$ * $P < 0.05$, ns, not significant. All statistical data were determined based on one-way ANOVA and Dunnett's post-hoc test. The enzymatic activities of urease, laccase, acid phosphatase, cellulase, and α-amylase in soluble cell lysates and culture supernatants were measured as described in the Materials and Methods section. (G) Analysis of the conventional secretion of Cda1 in *C. neoformans*. Presence of Cda1 was analyzed in total (T), soluble (S), and insoluble (I) fractions of intracellular extracts (left), along with the secreted fraction (right). Subcellular fractionations were performed as previously described (Thak et al., 2022), and the fractions were subjected to western blotting analysis using an anti-Cda1 antibody. (H) Analysis of raffinose utilization as the carbon source. Spotting analysis was performed on *C. neoformans* WT, *ugg1*Δ, and *cap59*Δ strains cultivated in SC media with or without glucose or raffinose supplementation. Plates were incubated for 3 days at 30 °C.

Figure 8. Analysis of extracellular vesicles purified from WT, *ugg1*Δ, and *cap59*Δ cells

(A, B) Nanoparticle tracking analysis (NTA) of EVs extracted from WT, *ugg1*Δ, and *cap59*Δ strains and quantification of total extracellular vesicle (EV) concentration per cell density. Quantitative measurements were derived from three independent experiments with standard deviations presented as error bars. Statistical significance: *** $P<0.0005$, * $P< 0.05$. All statistical data were determined based on one-way ANOVA and Dunnett's post-hoc test. (C, D) Cryo-TEM imaging of purified EVs and comparative analysis of EV size in WT, *ugg1*Δ, and *cap59*Δ strains. Scale bar, 100 nm. Total number of 100 EVs per strain, as captured using cryo-TEM, were analyzed for measuring the outer EV diameter. (E) Heatmap representation of fold change between WT and *ugg1*Δ EV-associated proteins, commonly detected in this

study and in previously reported EV proteome datasets (*ugg1*Δ/WT). Upregulated proteins in *ugg1*Δ are shown in red, whereas downregulated proteins are shown in blue. (F) Blotting analysis of GXM in the *C. neoformans* cells and EVs of WT, *ugg1*Δ, and *cap59*Δ strains. The 8 M urea extracts were obtained from EVs and cell pellets, from which EVs are generated. The urea extracts (5 μg total proteins) were loaded on 8% SDS-polyacrylamide gel and subjected to silver staining or blotting analysis using the anti-GXM 18B7 (α-GXM) and anti-Cda1 (α-Cda1) antibodies, respectively. Left: total cell extract. Right: total EV extract.

Figure 9. Impact of ERQC disruption on glycoprotein folding and EV-mediated transport of virulence factors in *C. neoformans* (A) In WT strain, *C. neoformans* UGGT homolog, Ugg1, functions as a sensor for misfolded glycoproteins within the ER, playing a crucial role in protein quality control. Functional ERQC is essential not only for ensuring the proper folding of glycoproteins, which is critical for maintaining cellular fitness, but also for facilitating EV-mediated secretion of capsule polysaccharides and virulence-related enzymes necessary for pathogenicity. (B) In the UGGT-deficient strain (*ugg1*Δ), ER stress is increased because of misfolded protein accumulation within the ER lumen. This heightened stress leads to decreased cellular fitness, which negatively impacts EV biogenesis and cargo loading. Consequently, significant defect occurs in EV-mediated transport, which ultimately leads to a complete loss of virulence. Nc: nucleus, Vc: vacuoles

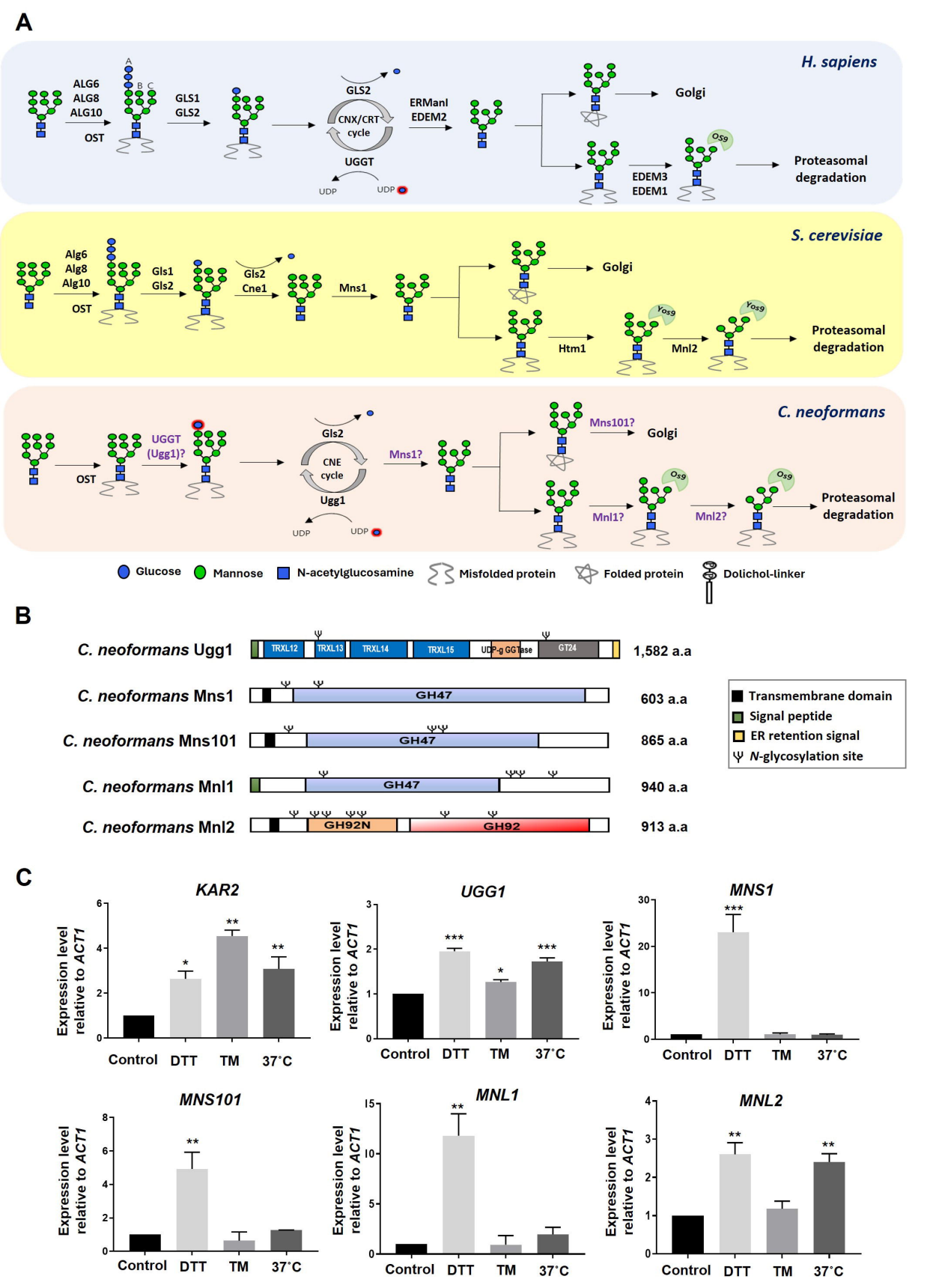
A
H. sapiens
ALG6
ALG8
ALG10
OST
A
B C
GLS1
GLS2
GLS2
CNX/CRT cycle
UGGT
UDP
UDP
ERManI
EDEM2
Golgi
EDEM3
EDEM1
Os9
Proteasomal degradation
S. cerevisiae
Alg6
Alg8
Alg10
OST
Gls1
Gls2
Gls2
Cne1
Mns1
Golgi
Htm1
Yos9
Mnl2
Yos9
Proteasomal degradation
C. neoformans
OST
UGGT (Ugg1)?
Gls2
CNE cycle
Ugg1
UDP
UDP
Mns1?
Mns101?
Golgi
Mnl1?
Os9
Mnl2?
Os9
Proteasomal degradation
Glucose
Mannose
N-acetylglucosamine
Misfolded protein
Folded protein
Dolichol-linker
B
C. neoformans Ugg1
TRXL12
TRXL13
TRXL14
TRXL15
UDP-g GGTase
GT24
1,582 a.a
C. neoformans Mns1
GH47
603 a.a
C. neoformans Mns101
GH47
865 a.a
C. neoformans Mnl1
GH47
940 a.a
C. neoformans Mnl2
GH92N
GH92
913 a.a
Transmembrane domain
Signal peptide
ER retention signal
N-glycosylation site
C
KAR2
UGG1
MNS1
MNS101
MNL1
MNL2
Expression level relative to ACT1
Control
DTT
TM
37˚C

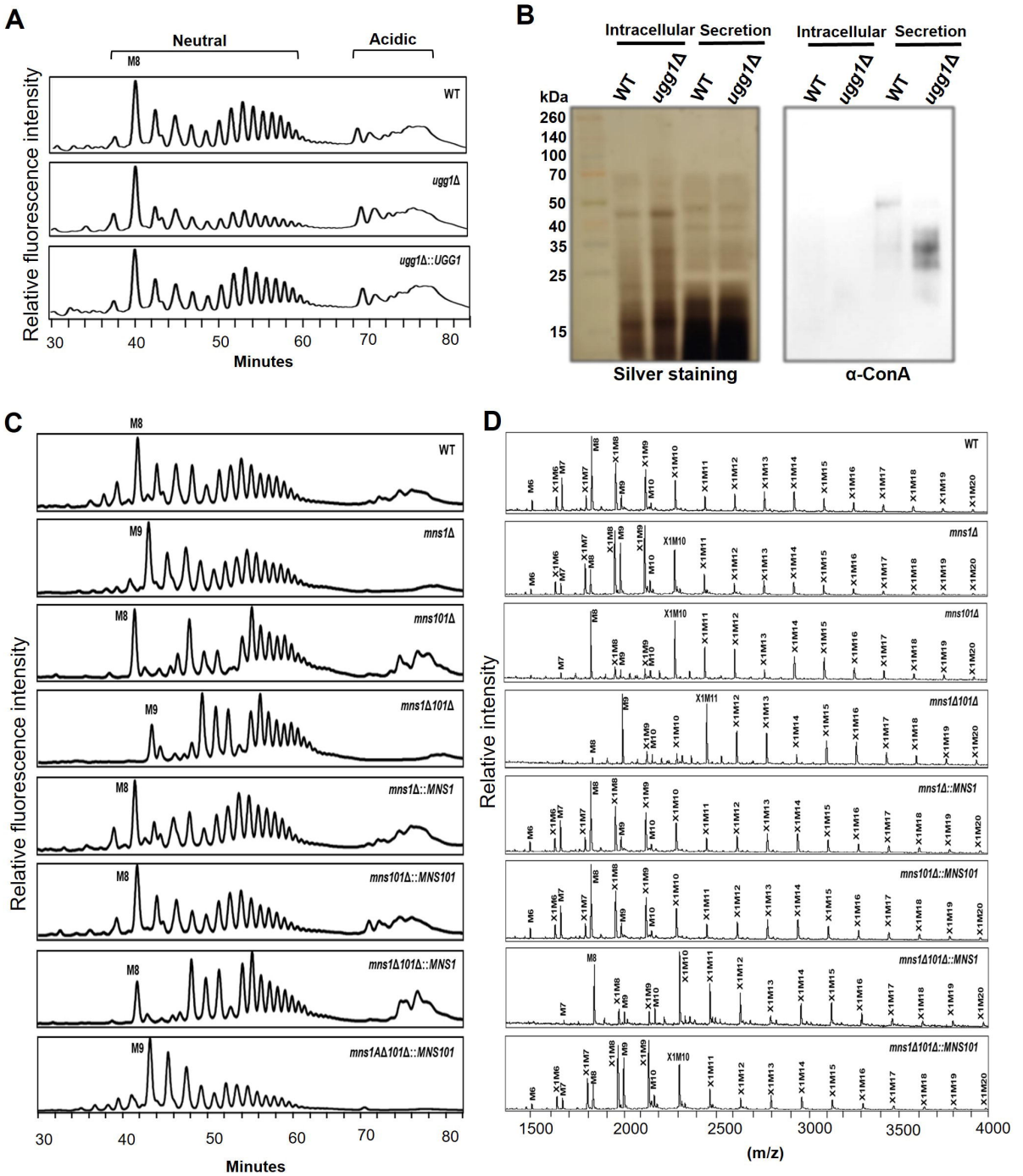
A
Neutral
Acidic
M8
WT
ugg1Δ
ugg1Δ::UGG1
Relative fluorescence intensity
30
40
50
60
70
80
Minutes
B
Intracellular
Secretion
WT
ugg1Δ
kDa
260
140
100
70
50
40
35
25
15
Silver staining
α-ConA
C
M8
M9
mns1Δ
mns101Δ
mns1Δ101Δ
mns1Δ::MNS1
mns101Δ::MNS101
mns1Δ101Δ::MNS1
mns1AΔ101Δ::MNS101
Relative fluorescence intensity
Minutes
D
M6
M7
X1M6
X1M7
X1M8
X1M9
X1M10
X1M11
X1M12
X1M13
X1M14
X1M15
X1M16
X1M17
X1M18
X1M19
X1M20
Relative intensity
1500
2000
2500
3000
3500
4000
(m/z)

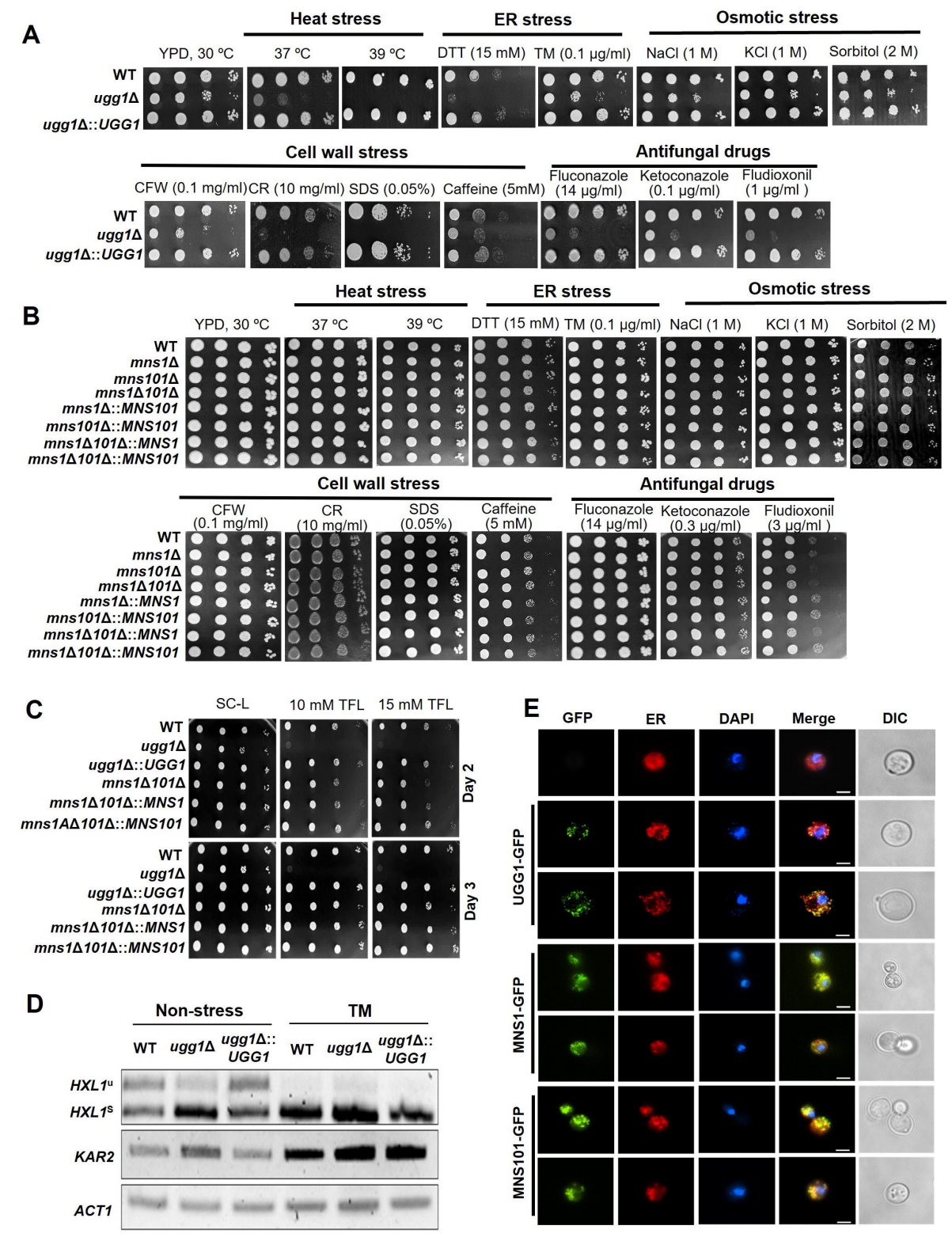
A
Heat stress
ER stress
Osmotic stress
YPD, 30 ºC
37 ºC
39 ºC
DTT (15 mM)
TM (0.1 μg/ml)
NaCl (1 M)
KCl (1 M)
Sorbitol (2 M)
WT
ugg1Δ
ugg1Δ::UGG1
Cell wall stress
Antifungal drugs
CFW (0.1 mg/ml)
CR (10 mg/ml)
SDS (0.05%)
Caffeine (5mM)
Fluconazole (14 μg/ml)
Ketoconazole (0.1 μg/ml)
Fludioxonil (1 μg/ml)
B
Heat stress
ER stress
Osmotic stress
YPD, 30 ºC
37 ºC
39 ºC
DTT (15 mM)
TM (0.1 μg/ml)
NaCl (1 M)
KCl (1 M)
Sorbitol (2 M)
WT
mns1Δ
mns101Δ
mns1Δ101Δ
mns1Δ::MNS101
mns101Δ::MNS101
mns1Δ101Δ::MNS1
mns1Δ101Δ::MNS101
Cell wall stress
Antifungal drugs
CFW (0.1 mg/ml)
CR (10 mg/ml)
SDS (0.05%)
Caffeine (5 mM)
Fluconazole (14 μg/ml)
Ketoconazole (0.3 μg/ml)
Fludioxonil (3 μg/ml)
WT
mns1Δ
mns101Δ
mns1Δ101Δ
mns1Δ::MNS1
mns101Δ::MNS101
mns1Δ101Δ::MNS1
mns1Δ101Δ::MNS101
C
SC-L
10 mM TFL
15 mM TFL
WT
ugg1Δ
ugg1Δ::UGG1
mns1Δ101Δ
mns1Δ101Δ::MNS1
mns1AΔ101Δ::MNS101
Day 2
WT
ugg1Δ
ugg1Δ::UGG1
mns1Δ101Δ
mns1Δ101Δ::MNS1
mns1Δ101Δ::MNS101
Day 3
D
Non-stress
TM
WT
ugg1Δ
ugg1Δ::UGG1
WT
ugg1Δ
ugg1Δ::UGG1
HXL1u
HXL1S
KAR2
ACT1
E
GFP
ER
DAPI
Merge
DIC
UGG1-GFP
MNS1-GFP
MNS101-GFP

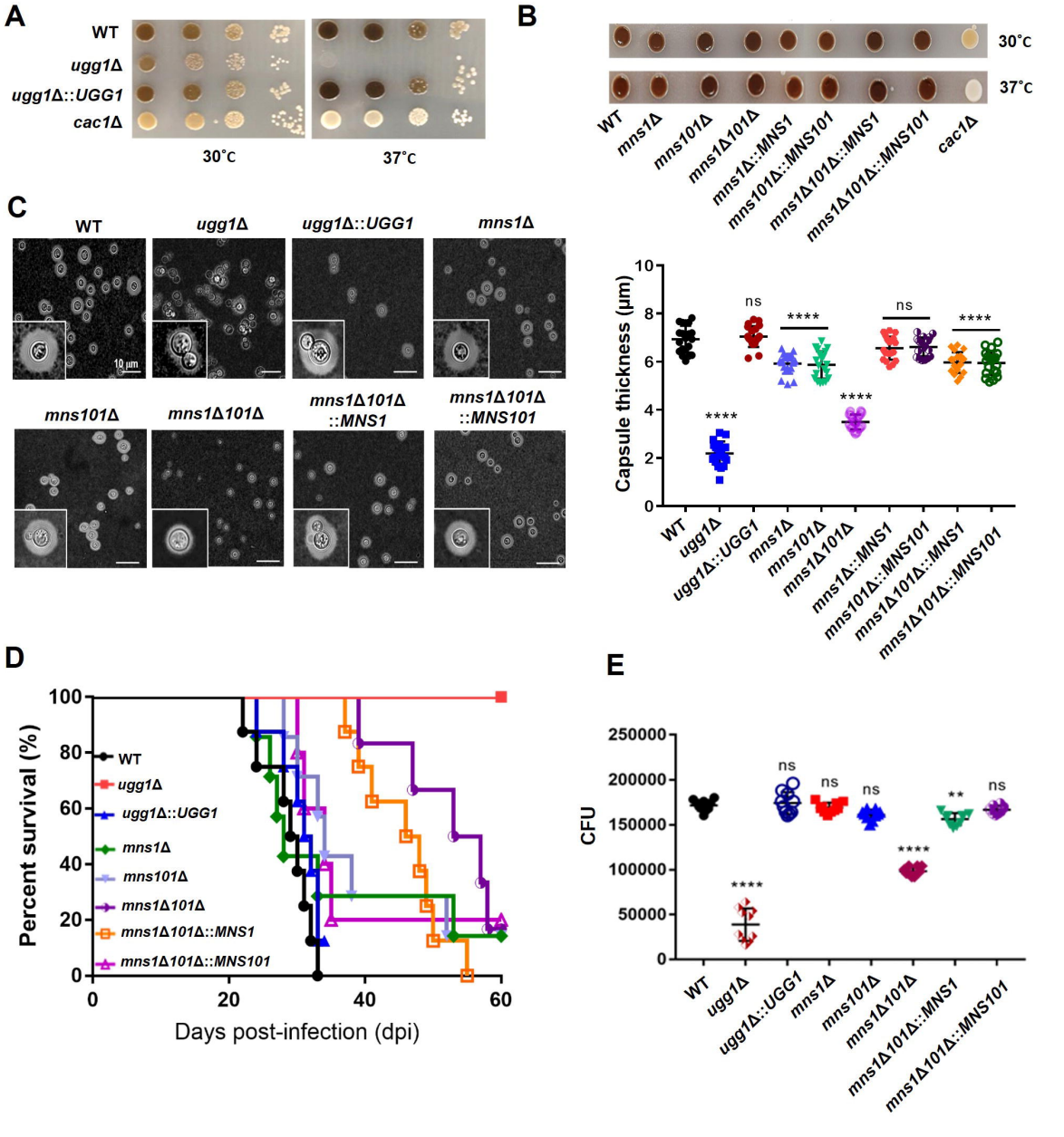
A
WT
ugg1Δ
ugg1Δ::UGG1
cac1Δ
30°C
37°C
B
30°C
37°C
WT
mns1Δ
mns101Δ
mns1Δ101Δ
mns1Δ::MNS1
mns101Δ::MNS101
mns1Δ101Δ::MNS1
mns1Δ101Δ::MNS101
cac1Δ
C
WT
ugg1Δ
ugg1Δ::UGG1
mns1Δ
10 μm
mns101Δ
mns1Δ101Δ
mns1Δ101Δ ::MNS1
mns1Δ101Δ ::MNS101
Capsule thickness (μm)
ns
****
WT
ugg1Δ
ugg1Δ::UGG1
mns1Δ
mns101Δ
mns1Δ101Δ
mns1Δ::MNS1
mns101Δ::MNS101
mns1Δ101Δ::MNS1
mns1Δ101Δ::MNS101
D
Percent survival (%)
Days post-infection (dpi)
WT
ugg1Δ
ugg1Δ::UGG1
mns1Δ
mns101Δ
mns1Δ101Δ
mns1Δ101Δ::MNS1
mns1Δ101Δ::MNS101
E
CFU
ns
**
****
WT
ugg1Δ
ugg1Δ::UGG1
mns1Δ
mns101Δ
mns1Δ101Δ
mns1Δ101Δ::MNS1
mns1Δ101Δ::MNS101

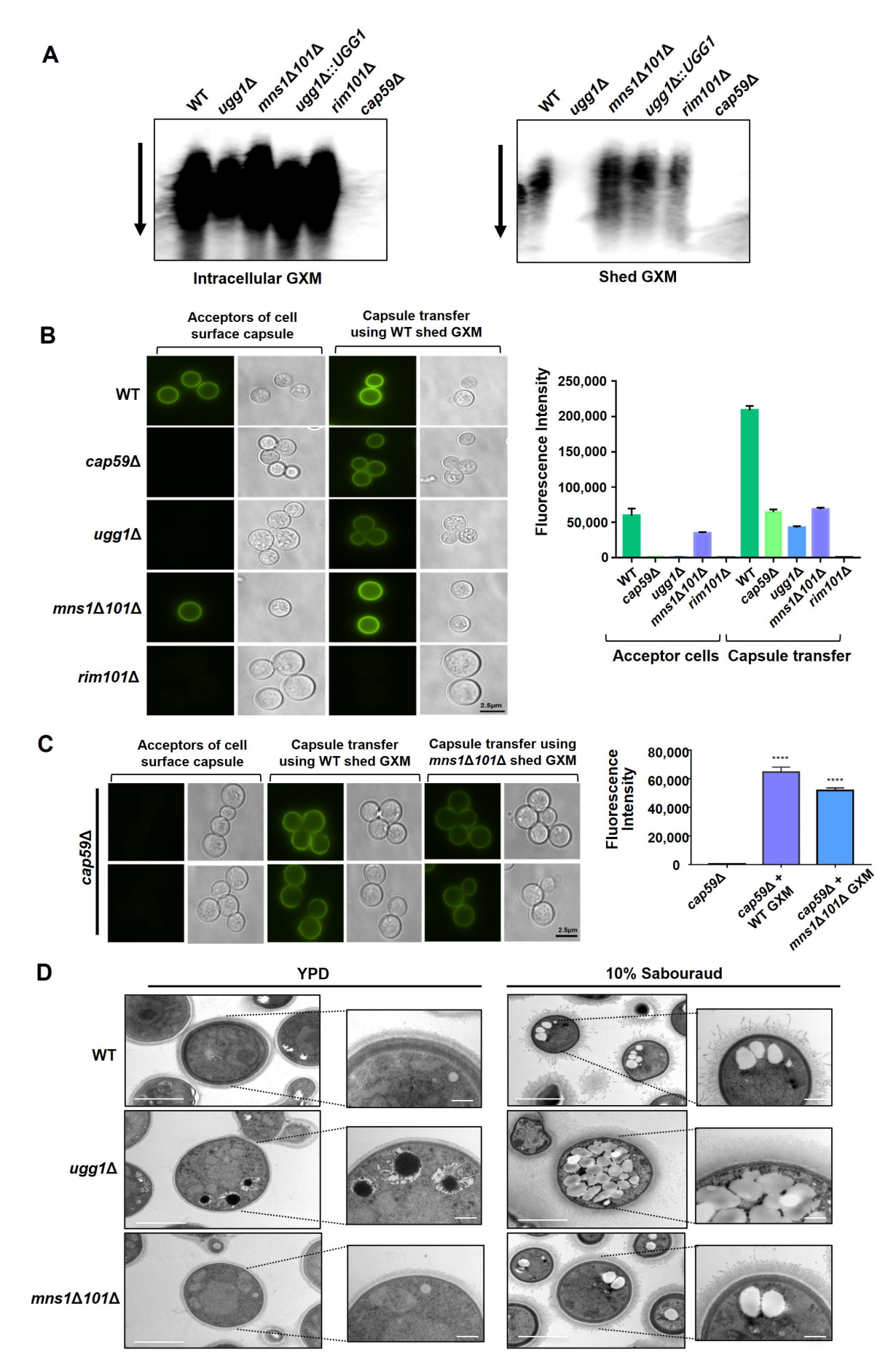
A
WT
ugg1Δ
mns1Δ101Δ
ugg1Δ::UGG1
rim101Δ
cap59Δ
Intracellular GXM
Shed GXM
B
Acceptors of cell surface capsule
Capsule transfer using WT shed GXM
WT
cap59Δ
ugg1Δ
mns1Δ101Δ
rim101Δ
2.5μm
Fluorescence Intensity
250,000
200,000
150,000
100,000
50,000
0
Acceptor cells
Capsule transfer
C
Acceptors of cell surface capsule
Capsule transfer using WT shed GXM
Capsule transfer using mns1Δ101Δ shed GXM
cap59Δ
2.5μm
Fluorescence Intensity
80,000
60,000
40,000
20,000
0
****
cap59Δ + WT GXM
cap59Δ + mns1Δ101Δ GXM
D
YPD
10% Sabouraud
WT
ugg1Δ
mns1Δ101Δ

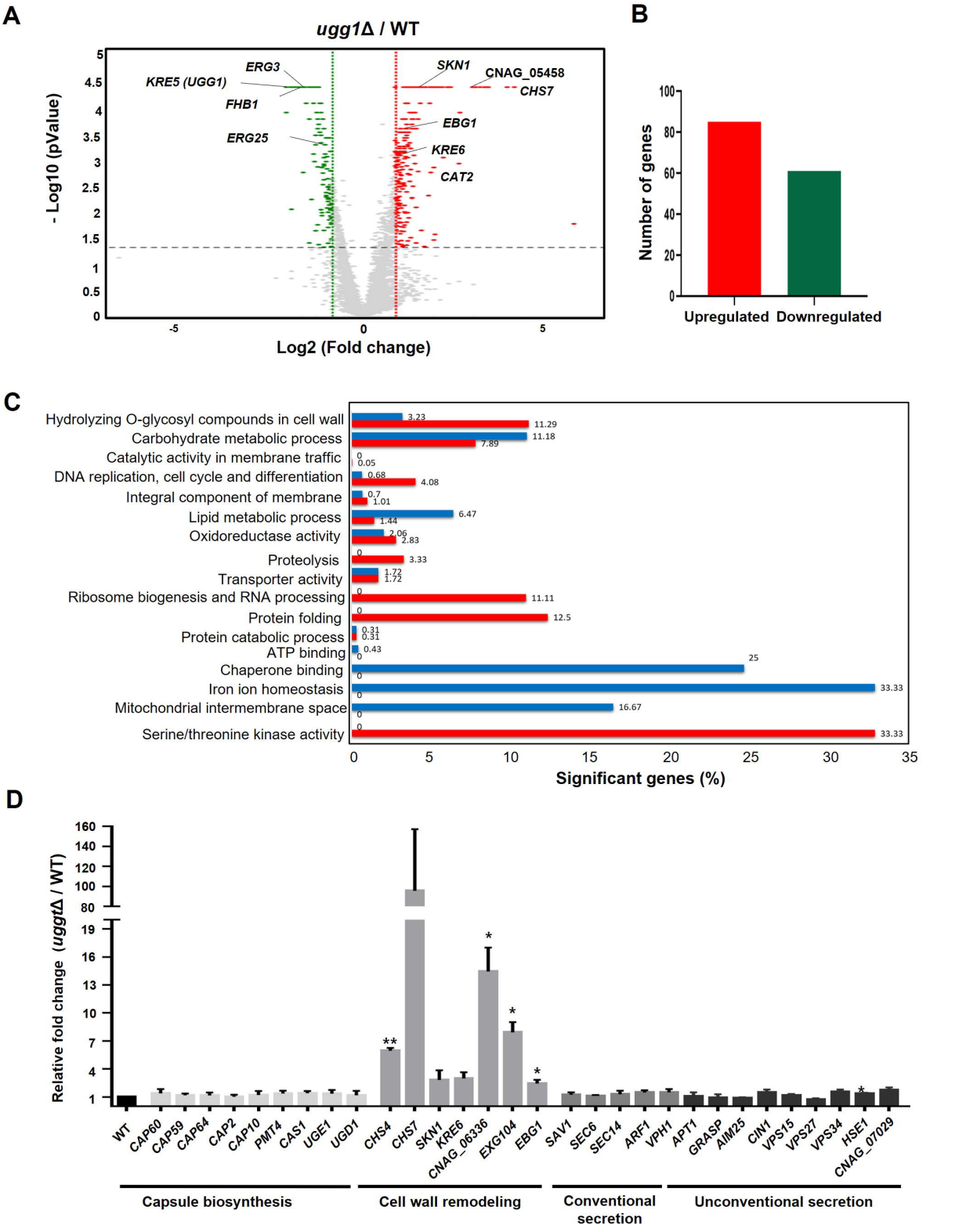
A
ugg1Δ / WT
- Log10 (pValue)
Log2 (Fold change)
ERG3
KRE5 (UGG1)
FHB1
ERG25
SKN1
CNAG_05458
CHS7
EBG1
KRE6
CAT2
B
Number of genes
Upregulated
Downregulated
C
Hydrolyzing O-glycosyl compounds in cell wall
Carbohydrate metabolic process
Catalytic activity in membrane traffic
DNA replication, cell cycle and differentiation
Integral component of membrane
Lipid metabolic process
Oxidoreductase activity
Proteolysis
Transporter activity
Ribosome biogenesis and RNA processing
Protein folding
Protein catabolic process
ATP binding
Chaperone binding
Iron ion homeostasis
Mitochondrial intermembrane space
Serine/threonine kinase activity
Significant genes (%)
D
Relative fold change (uggtΔ / WT)
WT
CAP60
CAP59
CAP64
CAP2
CAP10
PMT4
CAS1
UGE1
UGD1
CHS4
CHS7
SKN1
KRE6
CNAG_06336
EXG104
EBG1
SAV1
SEC6
SEC14
ARF1
VPH1
APT1
GRASP
AIM25
CIN1
VPS15
VPS27
VPS34
HSE1
CNAG_07029
Capsule biosynthesis
Cell wall remodeling
Conventional secretion
Unconventional secretion

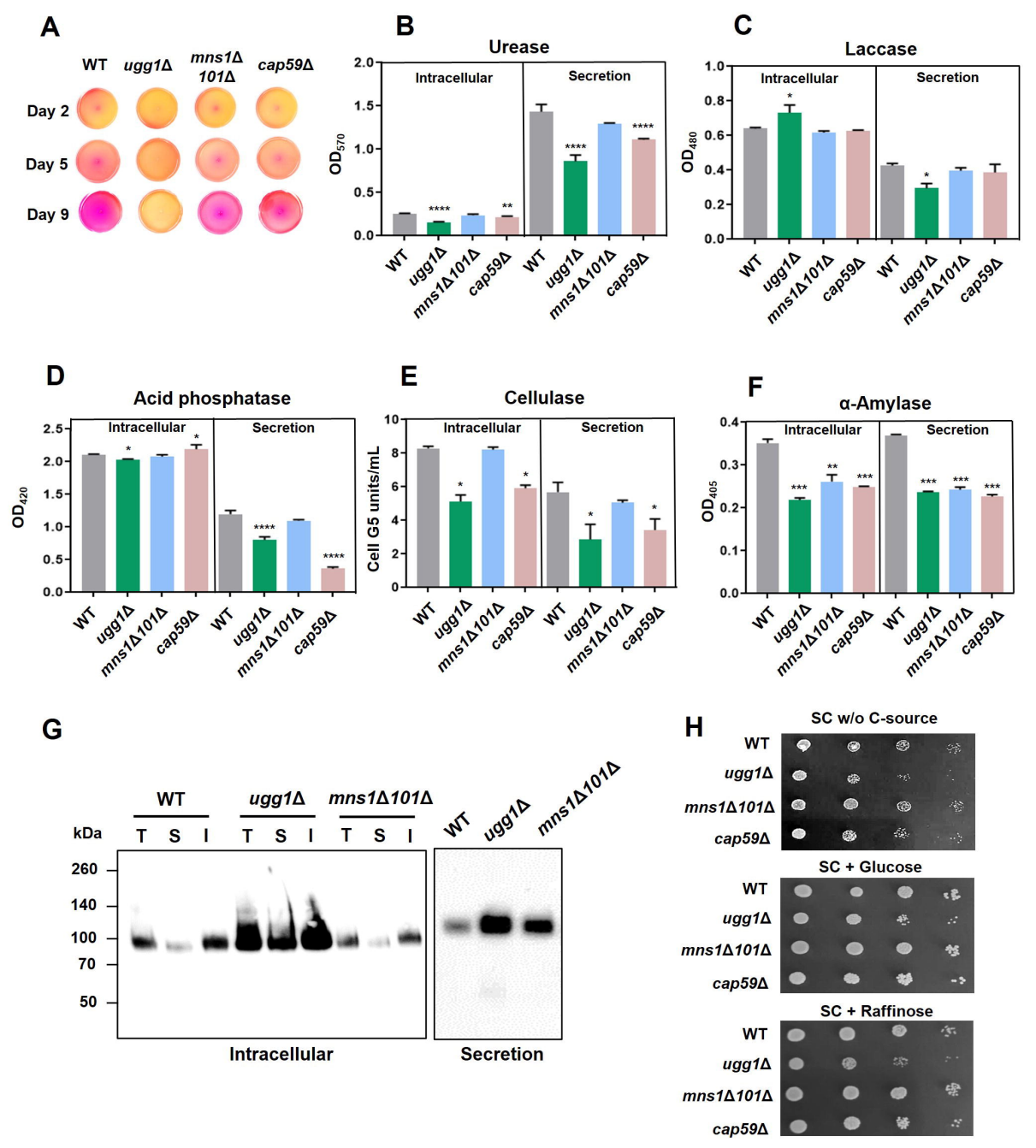
A
WT
ugg1Δ
mns1Δ 101Δ
cap59Δ
Day 2
Day 5
Day 9
B
Urease
Intracellular
Secretion
OD570
C
Laccase
OD480
D
Acid phosphatase
OD420
E
Cellulase
Cell G5 units/mL
F
α-Amylase
OD405
G
kDa
T S I
260
140
100
70
50
Intracellular
Secretion
H
SC w/o C-source
SC + Glucose
SC + Raffinose

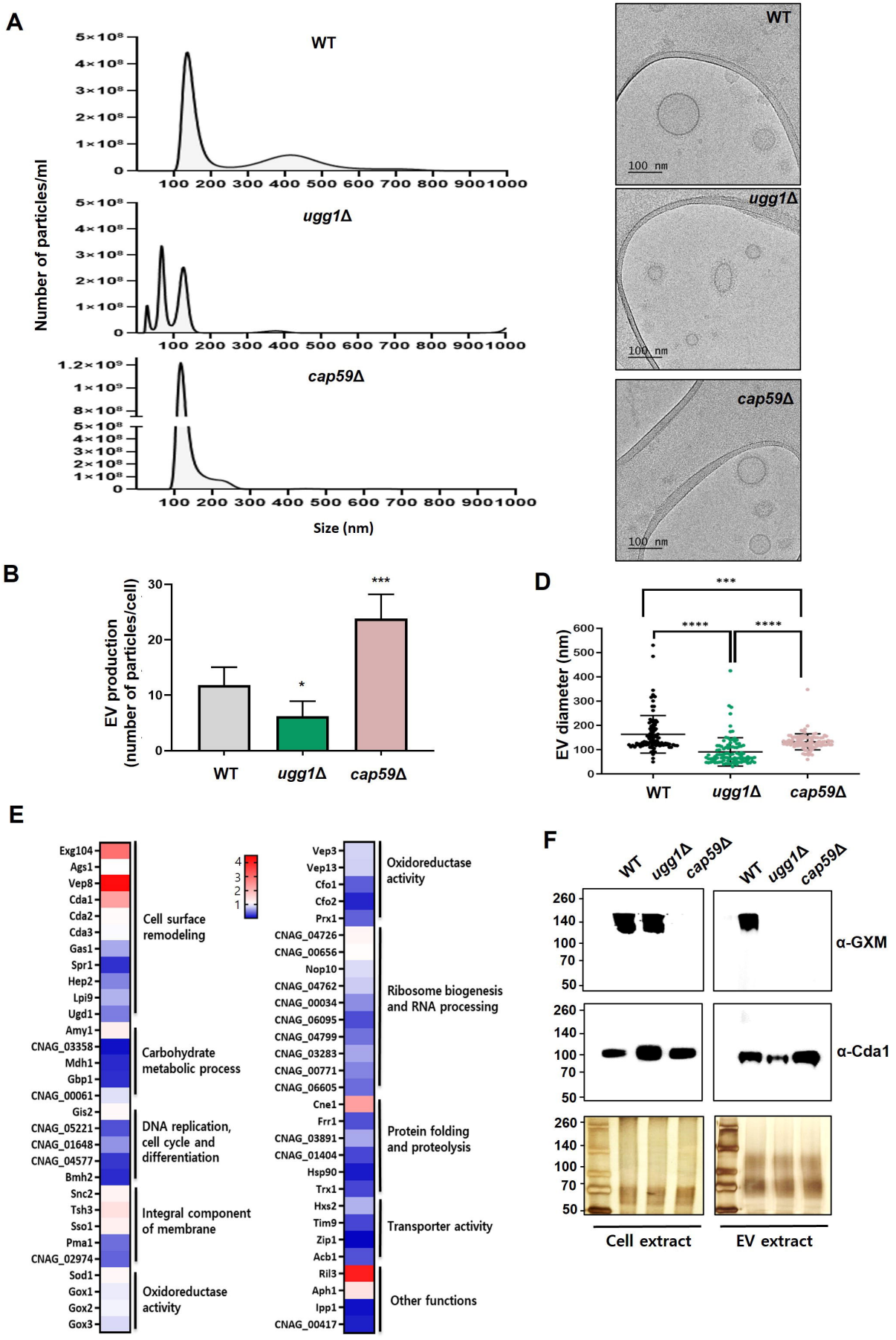
A
WT
ugg1Δ
cap59Δ
Number of particles/ml
Size (nm)
100 nm
B
EV production (number of particles/cell)
WT
ugg1Δ
cap59Δ
D
EV diameter (nm)
E
Cell surface remodeling
Carbohydrate metabolic process
DNA replication, cell cycle and differentiation
Integral component of membrane
Oxidoreductase activity
Ribosome biogenesis and RNA processing
Protein folding and proteolysis
Transporter activity
Other functions
F
α-GXM
α-Cda1
Cell extract
EV extract

49 Spadina Ave. Suite 200
Toronto ON M5V 2J1 Canada
www.biorender.com

Confirmation of Publication and Licensing Rights

July 25th, 2024
Science Suite Inc.

Subscription:	*Lab*
Agreement number:	*OD273NKXDN*
Journal name:	*eLife*

To whom this may concern,

This document is to confirm that Sam Skalet has been granted a license to use the BioRender content, including icons, templates and other original artwork, appearing in the attached completed graphic pursuant to BioRender's Academic License Terms. This license permits BioRender content to be sublicensed for use in journal publications.

All rights and ownership of BioRender content are reserved by BioRender. All completed graphics must be accompanied by the following citation: "Created with BioRender.com".

BioRender content included in the completed graphic is not licensed for any commercial uses beyond publication in a journal. For any commercial use of this figure, users may, if allowed, recreate it in BioRender under an Industry BioRender Plan.

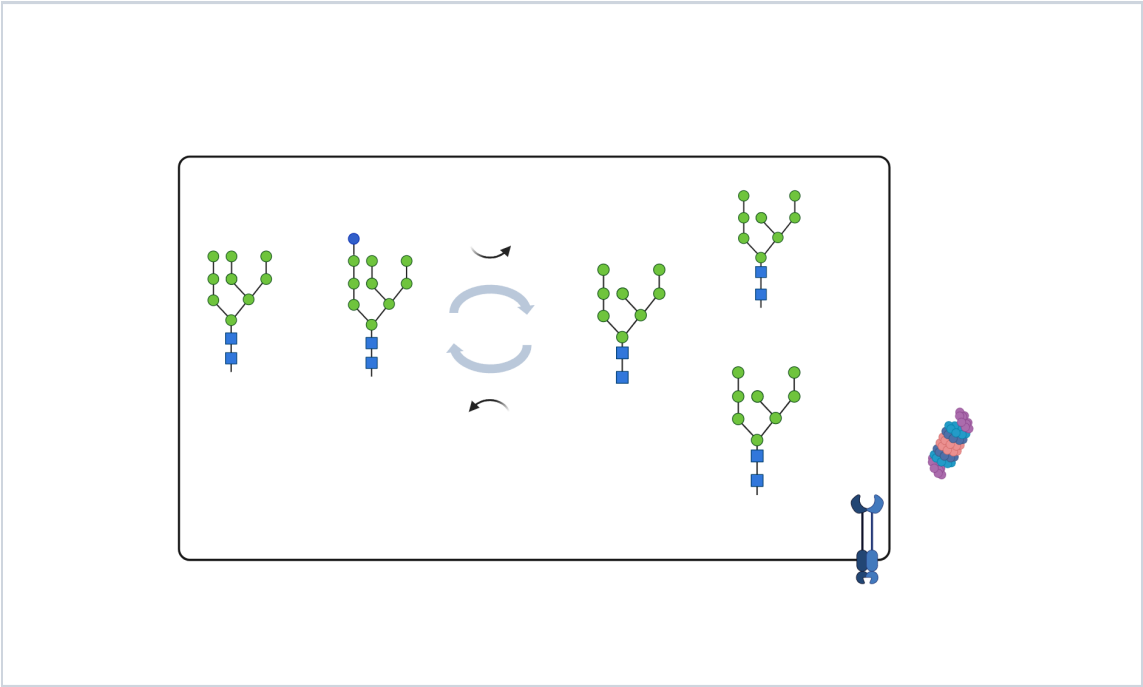

For any questions regarding this document, or other questions about publishing with BioRender refer to our BioRender Publication Guide, or contact BioRender Support at support@biorender.com.

49 Spadina Ave. Suite 200
Toronto ON M5V 2J1 Canada
www.biorender.com

Confirmation of Publication and Licensing Rights

July 25th, 2024
Science Suite Inc.

Subscription:	*Lab*
Agreement number:	*WR273NK5VX*
Journal name:	*eLife*

To whom this may concern,

This document is to confirm that Sam Skalet has been granted a license to use the BioRender content, including icons, templates and other original artwork, appearing in the attached completed graphic pursuant to BioRender's Academic License Terms. This license permits BioRender content to be sublicensed for use in journal publications.

All rights and ownership of BioRender content are reserved by BioRender. All completed graphics must be accompanied by the following citation: "Created with BioRender.com".

BioRender content included in the completed graphic is not licensed for any commercial uses beyond publication in a journal. For any commercial use of this figure, users may, if allowed, recreate it in BioRender under an Industry BioRender Plan.

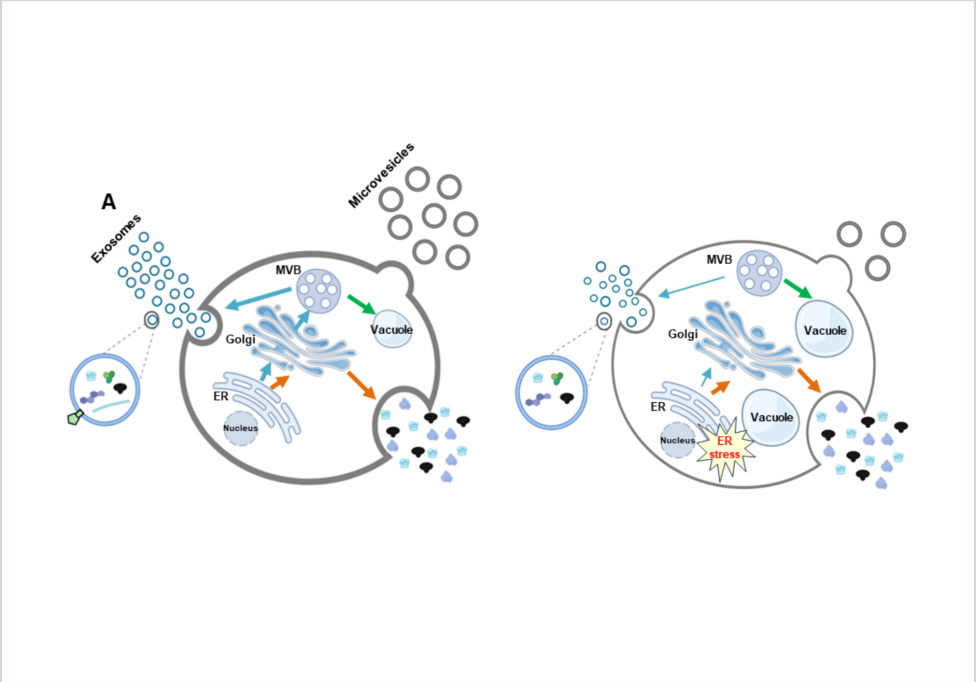

For any questions regarding this document, or other questions about publishing with BioRender refer to our BioRender Publication Guide, or contact BioRender Support at support@biorender.com.